CHAPTER 1: PHOTOINJECTOR THEORY

DAVID H. DOWELL
SLAC National Accelerator Laboratory
Menlo Park, CA 94025-7015
JOHN W. LEWELLEN
Naval Post Graduate School
Monterey, CA 93943

Keywords
RF Gun, RF Injector, Accelerator, Field Distribution, Beam Dynamics, Emittance, Brightness, Space Charge, Bunch Shape, Emittance Compensation, Chromatic Aberration, Geometric Aberration, Anomalous Field Aberration, Space Charge Shaping, Simulation Code, Injector Design Code, Particle-in-Cell Code, Envelope Code

Abstract
A comprehensive theory of photoinjectors involves a wide range of accelerator physics topics ranging from the material science of cathodes to the dynamics of electrons in magnetic, RF and DC fields as well as the strong effects the electrons have upon each other in their mutually repulsive fields, *i.e.* space charge fields. Whereas other chapters are concerned with subjects such as the physics of electron emission, this chapter concentrates upon electron beam dynamics from the cathode to the high energy accelerator after the gun. It briefly describes the history and components of the photoinjector as well as the basic beam parameters of emittance and brightness. The chapter then discusses beam dynamics without space charge (*i.e.* forces due to RF fields only), beam dynamics with space charge, the focusing and aberrations due to the magnetic solenoid lens and controlling beam quality with transverse shaping of the beam to eliminate non-linear space charge forces. The last section lists and describes the simulation codes available to the designers of photoinjectors. Two appendices giving tables of the chapter's formulae and mathematical symbols are included as a quick reference.

1.1 INTRODUCTION

Advances in the technology of high density, relativistic electron beams have made exciting new applications practical realities. A sampling of these new applications include Compton scattering sources, electron cooling of protons and heavy ions stored in a ring, energy recovery linac (ERL) light sources, free-electron lasers (FELs), inverse FELs and ultrafast electron diffraction. The first demonstration of a high average power FEL [1.1] and the operation of the first hard X-ray FEL as a 4th generation light source [1.2] represent two challenging fronts on the frontier of high brightness beam applications. Both of these achievements have benefited from the invention and continued development of the photoinjector.

This book's goal is to describe the technological components of these new photoinjectors from an engineering perspective. These technologies involve fields as diverse as RF power, high voltage (HV) DC, lasers, chemistry, ultra-high vacuum (UHV), beam optics, and others which are ably discussed by the authors of the other chapters and detailed by their references. It is the goal of this chapter to collect the various aspects of the theory of photoinjectors.

The photoinjector consists of a laser generated electron source followed by an electron beam optical system which preserves and matches the beam into a high-energy accelerator, as shown in Figure **1.1**. Matching the electron bunch to the first high-energy accelerator is one of the photoinjector functions, since the proper phase space sizing of the beam into the first accelerator section is an essential element of emittance compensation. In the low-energy regime of the photoinjector, the beam is considered to be "space charge dominated." In other words, its optical properties are strongly determined by the defocusing of space charge forces. Since the space charge forces are diminished as $(\textit{beam energy})^{-3}$, at relativistic energies, the electrons begin to follow ray optics and the beam is referred to as "emittance dominated."

The generic configuration of the photoinjector is shown in Figure **1.1**. The photoinjector consists of a cathode fabrication and/or transport system and electron gun, powered by RF (Chapter 10) or biased at a high voltage, beam optics for transporting and matching the beam to the high-energy accelerator, and assorted diagnostics (Chapter 11) and controls. The photocathode can be either a metal (Chapter 6) or one of several semiconductor materials (Chapters 7 and Chapter 8). The gun can be a high voltage DC gun (Chapter 4), a normal conducting RF (NCRF) gun (Chapter 2) or a superconducting RF (SCRF) gun (Chapter 3). In addition, it is necessary to suit the drive laser to the type of cathode and the desired pulse format (Chapter 9). Although there is a wide range of options for the cathode, laser and gun, the underlying beam physics is quite similar, as shown in the following sections of this chapter.

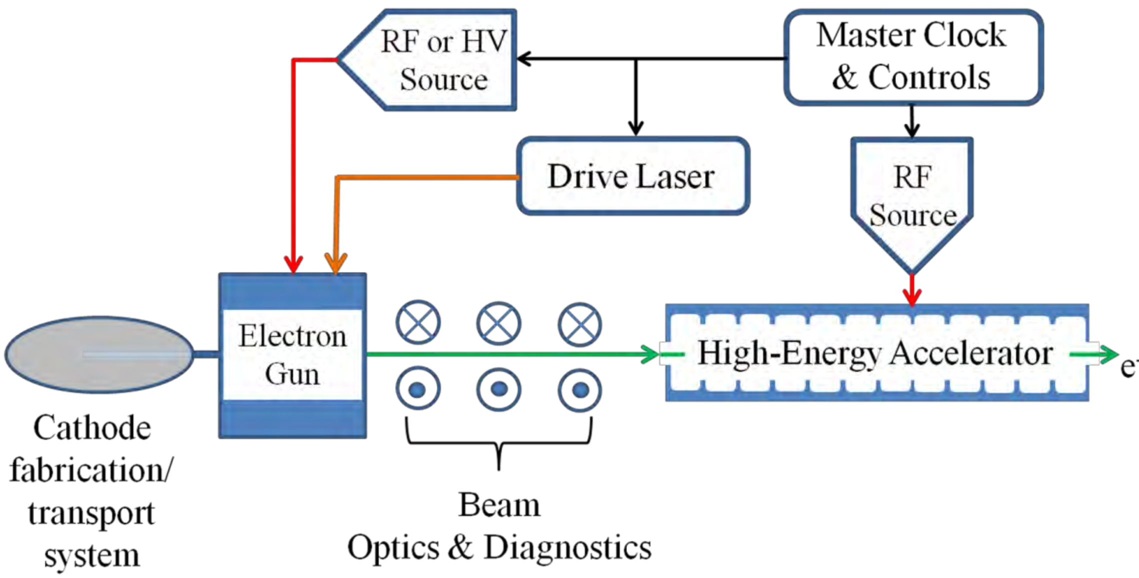

Figure 1.1. The parts of a photoinjector.

Electron beam quality is often specified in terms of three quantities: Emittance, peak current and brightness. The emittance is the area or volume of phase space the electrons occupy. In general, the phase space is the six dimensional space formed by an electron's three positions and angles. In 6-dimensional (6-D) space, the phase space coordinates are x, x', y, y', z and z'. Here, x, y and z are the electron position coordinates in the right-handed Cartesian coordinate system: the beam center is moving in the z-direction, the y-axis is vertical, and the x-axis pointing horizontal and to the left. The angles x', y' and z' are given by the momentum along that axis divided by the total momentum. For example, $x' = p_x/p_{total}$, where $p_{total}^2 = p_x^2 + p_y^2 + p_z^2$. Strictly speaking, the 6-D emittance should be computed from the electron distribution in the 6-D phase space. While this may be possible theoretically, in experiments the complete distribution details are not known and one can only measure projections of the distribution to find the emittance and other beam qualities. Projections of the 6-D phase space onto the 2-D sub-spaces of xx', yy' and zz' are called trace spaces.

The energy normalized trace space emittance is defined as

$$\varepsilon_n = \beta\gamma\sqrt{\langle x^2\rangle\langle x'^2\rangle - \langle xx'\rangle^2} \tag{1.1}$$

where $\beta = v\,c^{-1}$ is the electron velocity in units of the speed of light, c, and $\gamma = E_{total}/mc^2$ as the total beam energy, E_{total}, normalized to the electron mass, mc^2. Multiplying Equ. 1.1 by π gives the area of trace space occupied by the beam distribution, so it's often stated that the π is an "implied" factor in emittance unit. One can show that if there are no correlations between x, or x', and the other four coordinates that the trace space emittance in xx' trace space is conserved, that is $\langle xy\rangle = 0$, $\langle xy'\rangle = 0$ …, and similarly for the other trace spaces of yy' and zz'. However, correlations between the separate trace spaces lead to an increase in the trace space emittance. An example of a $\langle xyx'y'\rangle$ correlation is given in Section 1.5.4. Since it includes the effects of the correlations mixing of the trace spaces, the 6-D phase space emittance, often called the canonical emittance, remains unchanged. For the rest of this chapter, the trace space emittance will be referred to as the normalized transverse emittance, or simply the emittance.

The peak current, I_{peak}, is the bunch charge divided by the bunch length q_{bunch} and is usually calculated using the full-width at half-maximum (FWHM) bunch length. However, some authors compute it using the root mean squared (rms) or some other variant of the full width, or even reduce the charge to include only those electrons in the core of the bunch. In this book, we will use the total bunch charge and the FWHM bunch length. The peak current out of the gun should be as high as possible to avoid having to bunch the beam before acceleration in the high energy linac. The bunch length, and hence the peak current from the injector depends upon the RF frequency of the main accelerator since the bunch length should be a small fraction of an RF period. A sensible guideline is less than 10˚ RF[1] for the full bunch length. Hence, for a 3 GHz, linac the beam at the end of the injector should approximately have a maximum bunch length of 10˚ S or 10 ps. This then establishes a lower limit for the peak current at a given charge, ignoring bunch elongation. For example, at 1 nC the peak current from a 3 GHz gun would be 100 A. Most applications require I_{peak} to be 10-100 A from the injector.

The beam brightness combines the emittance and the peak current into a single parameter measuring the electron volume density. There are various definitions for beam brightness, each having its own merits. The common practice is to define the transverse, normalized beam brightness, B_n, as given by Equ. 4.2 in Chapter 4

$$B_n = \frac{2I}{\pi^2 \varepsilon_{n,x}\varepsilon_{n,y}} \tag{1.2}$$

Here $\varepsilon_{n,x}$ is the normalized xx' trace space emittance and $\varepsilon_{n,y}$ is the yy' trace space emittance. The peak current is the bunch charge divided by the bunch FWHM.

While Equ. 1.2 is commonly used to define the beam brightness, a more accurate representation of beam brightness would include the bunch length and energy spread. Similar to the transverse emittance, these

[1] In this book, we will denote the RF phase in degrees as "˚ RF" and the temperature in degrees Celsius as "˚C" to avoid the confusion of using "˚" for both. When discussing a specific RF frequency band, such as the S-band, the RF phase in degrees at the S-band frequency is given as "˚ S" and similarly for the other frequency bands.

longitudinal characteristics can be represented by the longitudinal emittance, which in its simplest form (ignoring any correlations) is the product of the bunch length, Δt, and energy spread, ΔE

$$\varepsilon_z = \sigma_z\, \sigma_{\Delta E/E} \tag{1.3}$$

Here, σ_z is the rms bunch length and $\sigma_{\Delta E/E}$ is the rms fractional energy spread. An alternative definition of the peak brightness would then be

$$B_{peak} = \frac{2q_{bunch}}{\pi^2 \varepsilon_{n,x}\varepsilon_{n,y}\Delta t \Delta E} = \frac{2q_{bunch}}{\pi^2 \varepsilon_{n,x}\varepsilon_{n,y}\sigma_t \sigma_E} \tag{1.4}$$

The factor of ‘2’ results from the integration over the 4-D trace space enclosed by a hyperellipsoid. [1.3]

1.1.1 The First Photocathode RF Gun

In 1985, it was demonstrated that a photocathode could survive while delivering high current densities of over 200 A cm^{-2}. [1.4][1.3] This was rapidly followed by the first operation of a photocathode gun at Los Alamos National Laboratory as the electron source for an FEL experiment [1.5]–[1.7]. The gun was a single RF cell connected to a cross in which Cs_3Sb cathodes were fabricated on the end of a long stick which could be inserted into the gun. The laser beam was reflected from an in-vacuum mirror through the solenoids and gun and onto the cathode. Downstream of the gun, the beam emittance was measured using the pepper-pot technique and a magnetic spectrometer measured the energy and energy spread. While this demonstration showed the many advantages of improved beams from photocathodes, it also illustrated the difficulties of working with a cathode material which is often hard to fabricate and always sensitive to its environment.

1.1.2 Summary of Advances

The invention of the photoinjector motivated a large increase in the number of laboratories studying electron guns. In 1983, there were only 1 or 2 gun projects, but by 1990 there were more than 25 laboratories along with a few companies actively building and testing guns [1.8]. The immediate improvement in electron beam quality with the advent of the photocathode gun was then followed by a methodical pace of small but steady steps toward the current state-of-the-art. Figure **1.2** illustrates the history of the 1 nC bunched beam emittance over the past 50 years.

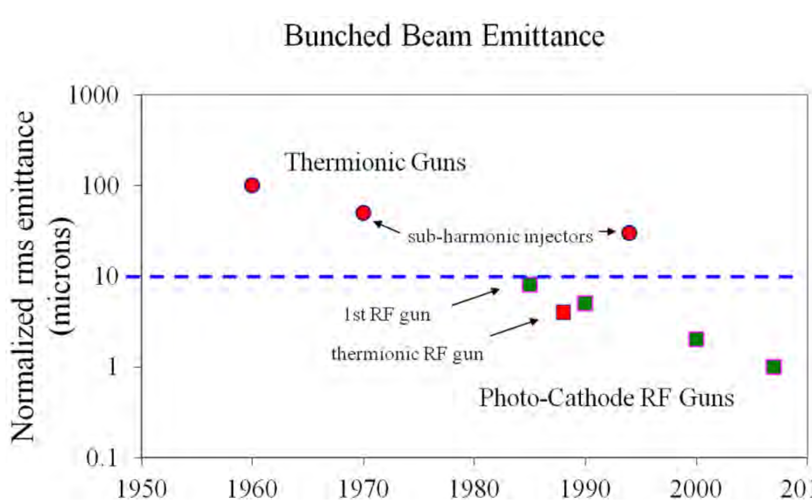

Figure 1.2. The demonstrated normalized emittance over the last 50 years for bunches compressed to 50 A to 100 A peak current.

The emittance is for a beam bunched from 50-100 A, since this is what's required for injection into a high energy linac. The projected emittance for 1 nC bunches is shown for thermionic and photocathode gun injector technologies in the figure. Thermionic guns were combined with sub-harmonic RF bunchers to achieve the 1 nC charge but could not achieve less than approximately 20 µm for the normalized emittance. In contrast even the first photocathode RF gun demonstrated better than 10 µm. This quick success was then followed by ~20 years of research to reach the goal of 1 micron at 1 nC.

In this book, we classify photoinjectors into three types: Normal Conducting RF (NCRF), Superconducting RF (SCRF) and high voltage DC (HV DC). There are one or more chapters devoted to each type. The proliferation and wide use of all three types of photoinjectors is illustrative of its success. Today there are more than a dozen facilities with NCRF guns, six operating or proposed SCRF guns and at least four using high brightness HV DC guns. A comparison of the beam emittance, charge, longitudinal phase space, repetition rate and other beam parameters for these three photoinjector types can be found in [1.9].

In addition, there are innovative injector designs which combine two or more of these three basic types of photoinjectors. A good example is the DC SCRF photoinjector at Peking University in Beijing. This system has a 90 kV HV DC gun placed close to the entrance of a 3½-cell SCRF accelerator and tries to combine the best features of the HV DC gun and the SCRF linac. [1.10]

The optimal RF frequency for the photocathode gun is often discussed, and it is often concluded that because higher frequencies produce higher electric fields that high frequencies should produce the best beam quality. There is no doubt that high electric field is important/essential for outrunning the space charge forces. However, there are other phenomena whose emittances scale upward with increasing RF field and frequency. For example, RF emittance is an unavoidable consequence of a gun with strong fields at a high RF frequency. As shown in Section 1.3, this emittance scales linearly with the peak electric field. Similarly, the emittance caused by the field enhancement due to rough cathode surfaces scales as the square root of the cathode field. Furthermore, for high average current injectors, the thermal management associated with high electric fields may even preclude operation in such a regime. Thus, high fields are not always advantageous.

Even with these advances, there remain opportunities for further improvements. Historically, the laser and the cathode have been the most problematic. However, recent developments in laser technology have resolved many of these issues. Diode-pumped solid state lasers now provide stable and reliable photons for photocathode guns. It is now possible to deliver the peak current required with a suitable choice of the cathode and the laser. Instead, further progress should concentrate on near the cathode. Improving the electron emission and mitigating the image and space charge effects will require a more complete understanding of the physical and chemical properties and reactions of the cathode material, both during fabrication and use in the gun. The goal is to develop cathodes with reliable and improved performance. The current cathode technology is discussed in Chapters 5 and Chapter 7.

Once the electrons are liberated from the cathode, they experience strong self-fields (space charge limited emission and emittance), fields in the accelerating cavities (RF emittance), and fields of the transport optics, all of which degrade the beam quality (chromatic and geometric aberrations). Space charge emittance is produced by the self-mutual repulsion of the electrons in the bunch, which is aggravated by the backward attraction of the image charge. The space charge limit occurs when the image charge electric field equals and cancels the applied electric field. Space charge emittance takes on various forms, but is always driven by non-uniformities in the charge density. The variation in the longitudinal charge density deforms the bunch with a variation in divergence, and hence emittance along its length. Emittance compensation in an RF gun refers to balancing the space charge divergence by focusing these divergence variations into alignment and compensate for the linear space charge force. This is possible if the space charge force is linear and the space charge force can be made linear if one uses special bunch shapes, for example the “beer-can.” Non-linear space charge forces increase the emittance due to a non-uniform charge distribution. The non-linear emittance usually cannot be corrected and instead is avoided by making the emission uniform.

The RF emittance results from the time-dependent focusing by the RF fields. The emittance of a thin time-slice of the bunch is unchanged and the slice merely obtains a change in divergence or an instantaneous kick in angle, as it would in a thin lens. However, the varying RF field gives a different divergence to each time-slice, which increases the projected emittance of the entire bunch. The RF emittance has a first- and second-order dependence upon the bunch length. This emittance is usually minimized by operating with short bunch lengths and optimal timing of when the laser produces the bunch with respect to the RF fields.

Since the gun itself acts as a strong defocusing lens, an equally strong focusing lens is needed to refocus the beam. This lens is usually a solenoid whose axial field focuses the electrons. Like all strong lenses this solenoid can produce a chromatic emittance due to the bunch energy spread and geometric emittance due to the transverse size.

This chapter attempts to discuss these effects with simple mathematical models. These models attempt to capture the underlying physics of the effects while providing useful formulas for estimating their contribution to the emittance. However, they are not meant to replace the need for numerical simulations using advanced multi-particle and mesh codes. The codes allow inclusion of the field shape and electron distribution minutia.

1.1.3 Organization of this Chapter

This chapter discusses the analytic theory of photocathode RF guns. It does this through the use of analytic models which accurately describe the physical phenomena for each portion of the photocathode gun system. The chapter begins with the definition of a photoinjector in Section 1.2. It is important to realize that producing a good beam from the cathode and gun is only the first part of emittance preservation of a larger system. There is also the matching of the beam into the first accelerator section and the damping of the emittance.

A discussion of beam dynamics without space charge forces is given in Section 1.3. The first- and second-order transverse RF emittances are derived and their relative sizes compared. The longitudinal emittance due to the RF is also computed.

Section 1.4 gives the space charge emittance for cylindrical (beer can) and Gaussian charge distributions. Analytic formulae are derived for both uniform and spatially varying transverse charge distributions. Space charge limited emission for a photocathode gun is shown to be different from the Child-Langmuir law. And a simple space charge model is given for non-uniform transverse emission. Emittance compensation is expressed in Section 1.4.4 in terms of a plasma oscillation being matched to the first linac section for minimum projected emittance. In a sense, this could be referred to as slice dynamics, given that it involves manipulating the slice parameters to make them the same.

Section 1.5 begins describing a linear optical model for the gun and solenoid. It then continues into an analysis of the solenoid's aberrations. The aberrations considered are chromatic, geometric and anomalous-quadrupole field. The anomalous-quadrupole field aberration results from a low strength quadrupole field which strongly couples the *x*- and *y*-emittances because of the large rotation angle in the solenoid. A means for "recovering" this emittance using normal and skew corrector quadrupoles is given.

The interesting and important topic of space charge shaping is presented in Section 1.6. Here, fundamental electromagnetic theory is used to compute ideal shapes with minimal non-linear space charge force. Often referred to as the "blow-out" regime, the linearization phenomenon is actually achieved by shaping the radial charge distribution so as to make the higher order space force terms zero.

The last section, Section 1.7, describes the capabilities of beam simulation codes. Sophisticated simulations allow high resolution computation of nearly all the details of the gun, solenoid and beamline components. And while the theory and models presented in the proceeding sections are important for understanding concepts and trends, all realistic gun designs require simulations with all the fine details.

1.2 THE RF PHOTOINJECTOR

1.2.1 The Photocathode RF Gun, Drive Laser and First Accelerator Section

A typical photocathode RF system shown in Figure **1.3** depicts a 1½-cell gun with a cathode in the ½ cavity being illuminated by a laser pulse train. At the exit of the gun is a solenoid which focuses the divergent beam from the gun and compensates for space charge emittance. The drive laser is mode-locked to the RF master oscillator which also provides the RF drive to the klystron. Other types of RF sources used to power RF guns are inductive output tube (IOT) and solid state RF amplifiers. (Not shown is the high voltage power supply powering the klystron.) How the RF power is coupled into the gun is an important technical aspect of the gun design. At high RF frequency, the coupling can be through the side-wall of one of the cavities with the cell-to-cell RF coupled through the irises between the cavities. Alternatively, the power can be coupled using coaxial coupler either at the beam exit or around the cathode [1.11]–[1.13]. At low frequencies, the RF can be launched using a coaxial cable [1.14]. These and other coupling schemes for NCRF guns are described in Chapters 2 and Chapter 10.

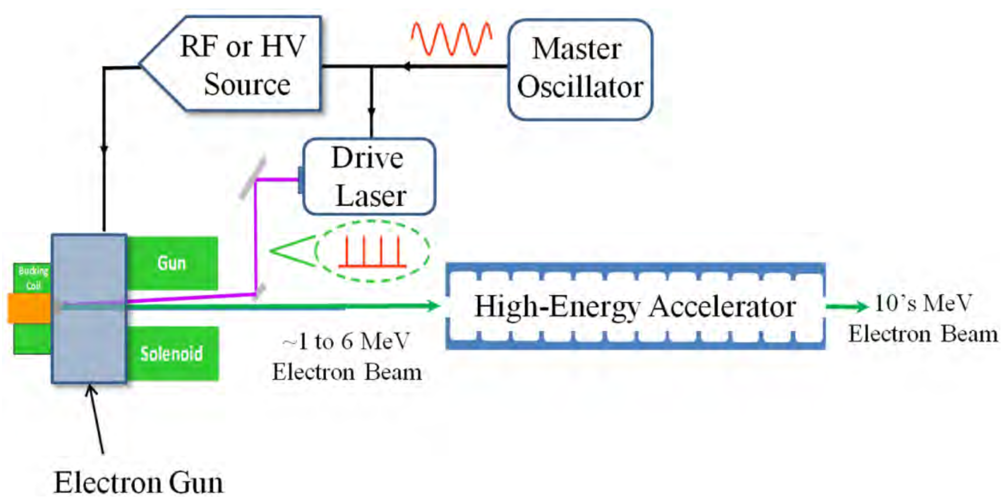

Figure 1.3. Basic components of the photocathode RF gun injector.

Equally important as the high field RF gun, cathode and laser is the optical matching of the beam size and divergence into the first linac section. The distance between the end of the gun and the entrance to the linac is determined by the bunch's plasma oscillation period. As discussed in Section 1.4.4, the bunch is matched when all the slices are aligned in transverse phase space, *i.e.*, have equal phase space parameters.

1.2.2 The ERL Injector System

Beam matching to the main linac is straightforward for a single pass accelerator. However, it becomes more problematic for circular machines, such as ERLs. In these accelerators, the spent, high-energy beam is decelerated in the same linac sections which accelerated them. Since ERLs are designed to operate at high average current, it is best to merge and un-merge the beam at beam energies which are below the neutron threshold of commonly used beam dump materials. Since neutron thresholds of most materials are from 10-15 MeV, 10 MeV is taken as the upper beam energy for the merger.

Due to the low beam energy and the relatively high peak current, there are significant space charge forces and other non-linear effects which can increase the emittance in the beam transport of the merger. Similar to emittance compensation technique, any emittance growth due to a correlation along the length of the bunch can be compensated for. The theory for the generalized dispersion produced by space charge dominated beams in bends has been developed in some detail for a merger with bi-lateral symmetry called the "zigzag" [1.15]. Here, this important topic is only briefly discussed for ERL mergers and the interested reader is directed to the references [1.16].

1.3 BEAM DYNAMICS WITHOUT SPACE CHARGE

1.3.1. RF Fields and Gun Geometries

The photocathode RF gun consists of a cathode in a half length cavity only, or the cathode ½-cell followed by one or more full length cavities. These cavities operate typically in a TM_{011} transverse magnetic mode. Figure **1.4** shows the cell structure for a 2½-cavity gun. Full cells are added to raise the beam energy out of the gun.

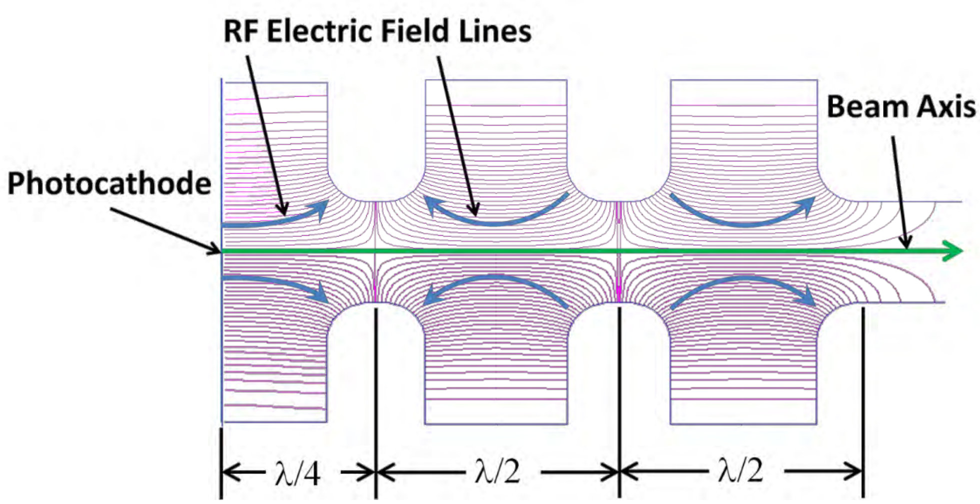

Figure 1.4. Field lines in a 2½-cell photocathode gun.

Figure **1.5** shows two commonly used geometries for the cell shape: Pillbox and re-entrant. The drawing on the left shows a pillbox cell, $\lambda/4$ long, creating the single cell pillbox RF gun. The re-entrant cavity shown on the right has higher shunt impedance than the pillbox and therefore has higher accelerating fields for the same RF power. However as a disadvantage, the reentrance shape has larger off-axis radial fields which can degrade the beam quality, but this effect is usually small. It is also more difficult to fabricate. On the other hand, the pillbox shape allows more freedom on the cathode design. This is advantageous in high voltage, high frequency guns where the cell wall itself is used as for the cathode. In one common design, the BNL/SLAC/UCLA gun, the entire cavity wall with the cathode is replaceable. This is a useful feature since it allows placing the RF joint at the outer circumference of the cavity where the magnetic field or surface current is high, but the electric field is low. This reduces the likelihood of high voltage arcing, although it does require good electrical contact to avoid resistive heating. In the reentrant cavity, the cathode is usually a plug inserted into the nose cone as shown in the figure. This adds to the complication of the reentrant design. A more extensive discussion comparing these two cavity shapes is given in Chapter 2.

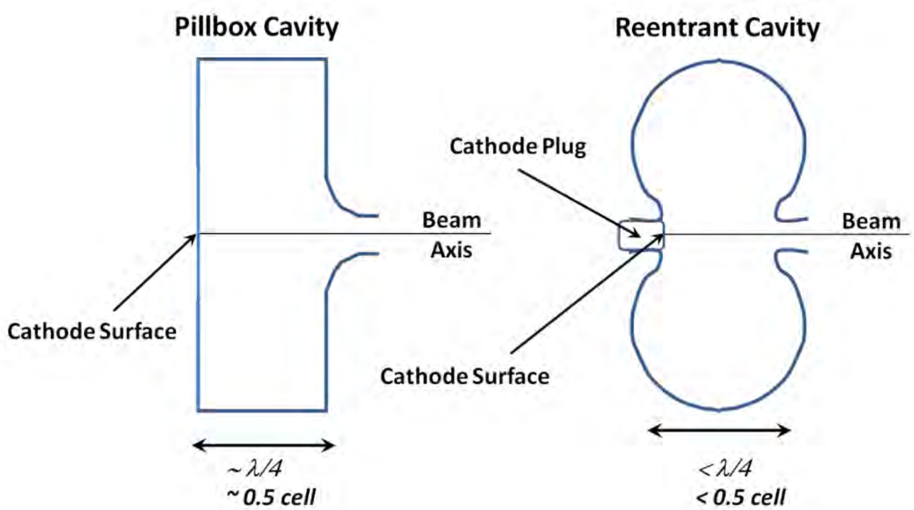

Figure 1.5. The two common geometries for the RF gun half cavity: Pillbox (left) and re-entrant (right).

Since we wish to accelerate electrons, the relevant modes are those with large longitudinal electric fields as shown in Figure **1.4**. These are the transverse magnetic (TM) modes. Writing out the electric and magnetic field components of the transverse magnetic modes, TM_{mnp}, of a pillbox cavity gives

$$E_z = E_0 J_m(k_{mn} r) \cos(m\theta) \cos(pk_z z) \exp[i(\omega t + \phi_0)] \tag{1.5}$$

$$E_r = -p \frac{k_z}{k_{mn}} E_0 J'_m(k_{mn} r) \cos(m\theta) \sin(pk_z z) \exp[i(\omega t + \phi_0)] \tag{1.6}$$

$$E_\theta = -mp \frac{k_z}{k_{mn}^2 r} E_0 J_m(k_{mn} r) \cos(m\theta) \sin(pk_z - z) \exp[i(\omega t + \phi_0)] \tag{1.7}$$

$$B_z = 0 \tag{1.8}$$

$$B_r = \frac{-i\omega m}{k_{mn}^2 c^2 r} E_0 J_m(k_{mn} r) \sin(m\theta) \cos(pk_z z) \exp[i(\omega t + \phi_0)] \tag{1.9}$$

$$B_\theta = \frac{-i\omega}{k_{mn} c^2} E_0 J'_m(k_{mn} r) \cos(m\theta) \cos(pk_z z) \exp[i(\omega t + \phi_0)] \tag{1.10}$$

These expressions assume the longitudinal origin at $z = 0$ is the cathode position. Here, E_0 is the field normalization, J_m is the mth-order Bessel function, k_{mn} is the nth zero of the mth-order Bessel function, R_{cavity} is the internal radius of the cavity and ω is the RF angular frequency. k_z is the longitudinal wave number, where $k_z = p\pi\, l^{-1}$, and l is the cavity length. The dispersion relation relates the frequency to the radial and longitudinal wave numbers

$$\frac{\omega^2}{c^2} = k_{mn}^2 + k_z^2 \tag{1.11}$$

The TM_{mnp} designation denotes the mode is transverse magnetic since $B_z = 0$. The m mode number refers to the azimuth angle, θ-dependence or rotational symmetry of the fields. Notice that the m mode number also affects the radial dependence of the fields through the Bessel functions J_m and their derivatives. Since we desire to produce a beam with rotational symmetry, $m = 0$ for all RF guns. The n mode number has been given above, and with the cavity radius gives the position of the radial nodes. The mode shape along the z-axis of the cavity is given by p. For reasons of timing and efficient acceleration, the full cell length for most RF guns is $\lambda/2$ and $p = 1$. The above mode equations then give a π phase shift between cells. Since the cathode is at a high field position, its cavity length is half that of a full cell, or $\lambda/4$. Numerical studies show that more optimal performance is obtained if the cathode cavity is 0.6X the full cell length, rather than 0.5. And finally these spatial functions of the mode oscillate with the RF frequency, ω, with a ϕ_0 phase or time shift between the beam and the fields.

Thus most RF guns use the TM_{011} mode whose non-zero field components are

$$E_z = E_0 J_0(k_{01}r)\cos(k_z z)\exp[i(\omega t + \phi_0)] \tag{1.12}$$

$$E_r = \frac{-k_z}{k_{01}} E_0 J_0'(k_{01}r)\sin(k_z z)\exp[i(\omega t + \phi_0)] \tag{1.13}$$

$$B_\theta = \frac{-ik_z}{k_{01}c} E_0 J_0'(k_{01}r)\cos(k_z z)\exp[i(\omega t + \phi_0)] \tag{1.14}$$

This mode is also called the π-mode, because the argument of the cosine function changes by π over a cell length. The fields for the π-mode oscillate at the same frequency, but with opposite sign. This cavity mode is often used for accelerators since the opposite field allows the electron bunch to catch the accelerating polarity of the field and remain synchronous with the accelerating field. Another mode is called the 0-mode has no phase change between the cells. For this mode, the fields oscillate in unison. Equ. 1.5 to Equ. 1.10 show there is no z-dependence with $p = 0$ for the TM_{010} mode.

The π-mode electric field for a 1.6-cell S-band RF gun is given in Figure **1.6**. The top of the figure shows the field lines computed by the SUPERFISH code [1.17] which includes the details of the cavity shape shown. The lower portion of the figure compares the longitudinal and transverse fields computed with SUPERFISH and with those given by Equ. 1.12 and Equ. 1.13. The differences in the field shapes are due to the presence of the beam ports and details of the cavity shape. All these effects are ignored in the analytic expressions. However, the pillbox formulae do capture the main features of the fields, and later in the chapter they are used to compute the beam's dynamics.

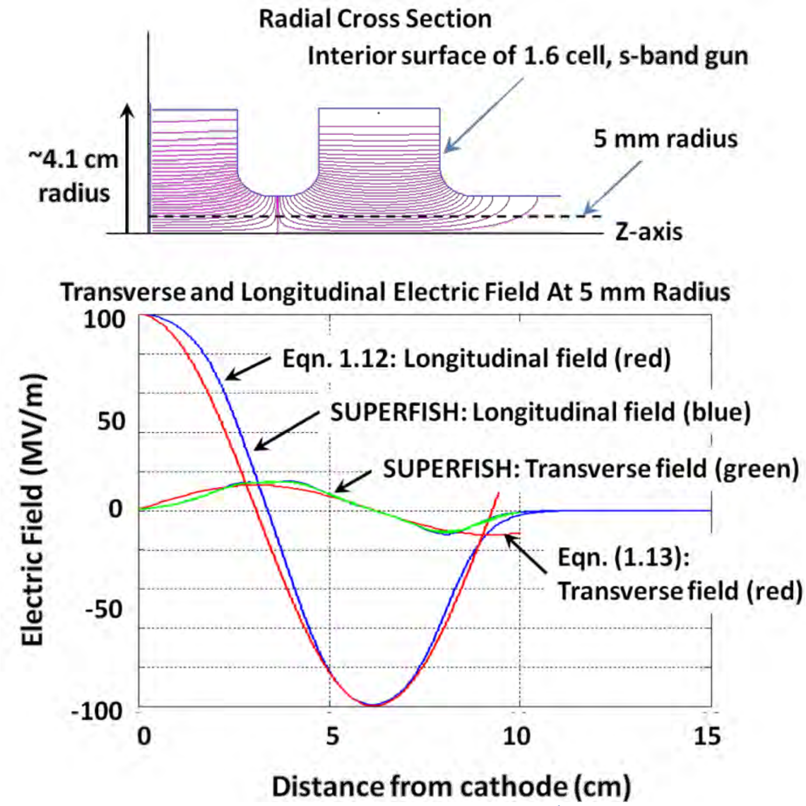

Figure 1.6. RF fields for an S-band gun operating at a peak field of 100 MV m^{-1} on the cathode. The upper portion of the figure is a cross section taken through the *r-Z* plane of a 1.6-cell, S-band gun showing the interior surface and the electric field lines. The field lines were computed by SUPERFISH [1.17] using the shown interior shape. The lower graph is a plot of the longitudinal and transverse electric fields at a radius of 5 mm as computed by SUPERFISH and given by Equ. 1.12 and Equ. 1.13.

1.3.2. Transverse Beam Dynamics in the RF Field

The radial force is

$$F_r = e(E_r - \beta c B_\theta) \tag{1.15}$$

and inserting Equ. 1.9 and Equ. 1.10 for the fields gives

$$F_r = e\frac{k_z}{k_{01}}E_0[\beta\cos(k_z z)\sin(\omega t + \phi_0) - \sin(k_z z)\cos(\omega t + \phi_0)]\, J_0'(k_{01}r) \tag{1.16}$$

We consider the RF transverse force at the two locations where it is the largest: The center iris and the gun exit iris. There is little transverse force near the cathode since the low electron velocity makes the first term small and the second term as well since it is proportional to $\sin(k_z z)$ and $z \approx 0$ near the cathode. We argue that the transverse force at the center iris is also negligible since for the π-mode the field $E_z(z)$ is anti-symmetric about the iris. However, the transverse force at the exit iris is significant since $E_z(z)$ doesn't change sign across the exit iris. Thus, the total transverse force is an impulse given at the exit iris, $z = z_f$. In addition, for most RF guns $\beta \approx 1$ at the gun exit, and assuming a small beam size allows us to write the force in the region of the gun exit as

$$F_r = -eE_0\frac{k_z r}{2}\sin(\omega t + \phi_0 - k_z z) \tag{1.17}$$

Next, we compute the change in radial momentum, p_r, using the equation of motion $\frac{\mathrm{d}p_r}{\mathrm{d}t} = \frac{F_r}{mc}$, where we're using Kim's definition of the dimensionless radial momentum $p_r = \frac{\gamma}{c}\frac{\mathrm{d}r}{\mathrm{d}t}$ [1.18]. The change in radial momentum is computed by integrating the force impulse over the position of the exit iris,

$$\Delta p_r = \frac{1}{mc^2}\int F_r dz = \frac{1}{mc^2}\int F_r(z)\delta\left(k_z\left(z - z_f\right)\right)dz \tag{1.18}$$

which gives

$$\Delta p_r = \frac{-eE_0}{mc^2} r\sin(\phi_e) \tag{1.19}$$

where $\phi_e = \omega t + \phi_0 - k_z z_f$. This is identical to Kim's expression although we began with the fields for the cylindrical pillbox cavity.

Following Kim, we convert from cylindrical to Cartesian coordinates to obtain the change in transverse momentum at the exit iris

$$\Delta p_x \equiv \beta\gamma x' = \frac{-eE_0}{2mc^2} x\sin(\phi_e) \tag{1.20}$$

Define the RF focal length in terms of the angular kick the beam gets at the exit of a cell,

$$x' = \frac{x}{f_{RF}} \tag{1.21}$$

which gives the focal length of the gun's RF lens as

$$f_{RF} = \frac{-2\beta\gamma mc^2}{eE_0 \sin(\phi_e)} \tag{1.22}$$

The RF focal strength can be quite strong for high field guns and for guns operating with high cathode field, but low exit energy. For example, for a gun operating at a peak field of 100 MV m^{-1} and exiting the gun on crest with an energy of 6 MeV results in a defocusing focal length of 12 cm. Thus, the beam out of a RF gun requires a focusing lens which is usually a solenoid lens. Details of the solenoid are discussed later in this chapter; however, since the length of the solenoid is ~20 cm, it's nearly the same as its focusing focal length the solenoid adds an aberration to the beam.

The emittance is increased by the gun's RF defocusing due to different longitudinal sections or slices of the electron bunch arriving at the exit iris at different RF phases. If we consider thin slices longitudinally along the bunch, we can see that they will have received different angular kicks by the RF, and thereby increase the overall emittance of the bunch. The projected emittance is the term used to describe this overall emittance and the term slice emittance refers to the emittance of a short longitudinal sliver of the beam. The electron bunch is typically divided into 10-15 slices whose emittance can be determined experimentally using a transverse RF cavity or other techniques, such as chirping the beam energy and using a spectrometer to disperse the slices.

The increase in the transverse phase space area is shown in Figure **1.7**. The xx' phase space is plotted for an exit phase of 0˚ are plotted as lines for the head (blue dash), tail (green dash) and the center (red solid) slices. The center slice (red solid) lies along the $x' = 0˚$ axis. Similar lines plotted along the diagonal line all lay on top of each other. The light shaded area illustrates the projected emittance for 0˚ which is much larger than the emittance for the 90˚ exit phase. This plot assumes the head-to-tail distance is 10˚.

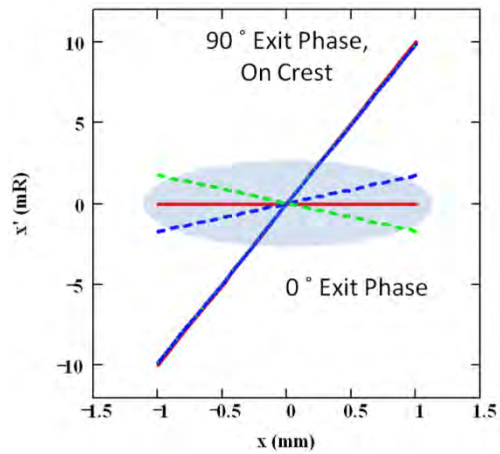

Figure 1.7. The transverse phase spaces of head, center and tail slices for exit phases of 0˚ and 90˚. The three slice phase spaces for 0˚ exit phase are plotted for the center slice (red-solid), head slice (blue dash) and the tail slice (green dash). The same color scheme is used for the 90˚ phase spaces which all lie on the same diagonal line. The linear (first-order) emittance for an exit phase of 90˚ is zero, as shown by the diagonal line.

The emittance can be computed beginning with the definition, $\varepsilon_n = \beta\gamma\sqrt{\langle x^2\rangle\langle x'^2\rangle - \langle xx'\rangle^2}$, which is normalized to the beam energy. For exit phases far from 90˚, the correlation term can be ignored

$$\varepsilon_n = \beta\gamma\sigma_x\sigma_{x'} \tag{1.23}$$

where σ_x is the rms beam size at the exit of the gun and $\sigma_{x'}$ is the rms divergence. We can estimate the angular dispersion from the variation of the divergence with the exit phase

$$\Delta x' = -\frac{\mathrm{d}}{\mathrm{d}\phi_e}\frac{1}{f_{RF}}\Delta x\Delta\phi_e \tag{1.24}$$

Taking the derivative of the focal strength and converting to rms beam size and bunch length at the exit iris gives the rms divergence

$$\sigma_{x'} = \frac{eE_0\cos(\phi_e)}{2\gamma mc^2}\sigma_x\sigma_\phi \tag{1.25}$$

and the first-order RF emittance is

$$\varepsilon_{RF}^{(1)} = \frac{eE_0\cos(\phi_e)}{2mc^2}\sigma_x^2\sigma_\phi \tag{1.26}$$

Near 90˚, the phase space becomes highly correlated, as shown in Figure **1.7**, and the first-order emittance goes exactly to zero at 90˚. However, there remains a quadratic emittance due to the RF curvature which is a maximum on crest. For a Gaussian longitudinal bunch then the emittance due to the RF curvature is [1.18]

$$\varepsilon_{RF}^{(2)} = \frac{eE_0 \left|\sin(\phi_e)\right|}{2\sqrt{2}mc^2}\, \sigma_x^2\sigma_\phi^2 \tag{1.27}$$

We can combine these expressions and write the total emittance for all values of ϕ_e as the quadratic sum of the first-order and second-order emittances

$$\varepsilon_{RF}^{total} = \frac{eE_0}{2mc^2}\, \sigma_x^2\sigma_\phi \sqrt{\cos^2(\phi_e) + \frac{\sigma_\phi^2}{2}\sin^2(\phi_e)} \tag{1.28}$$

Figure **1.8** graphs each of these emittances. The first-order RF emittance as a function of the exit phase becomes 0 on crest, or 90˚, where the second-order emittance is instead a maximum. The emittances shown have been calculated using a 4˚ rms (~10˚ FWHM) bunch length, a peak field of 100 MV m^{-1} and rms beam size of 1 mm. The second-order emittance can be cancelled using a higher RF harmonic [1.19]. This is similar to the linearization of the longitudinal phase space is done for bunch compressors using a harmonic cavity [1.20].

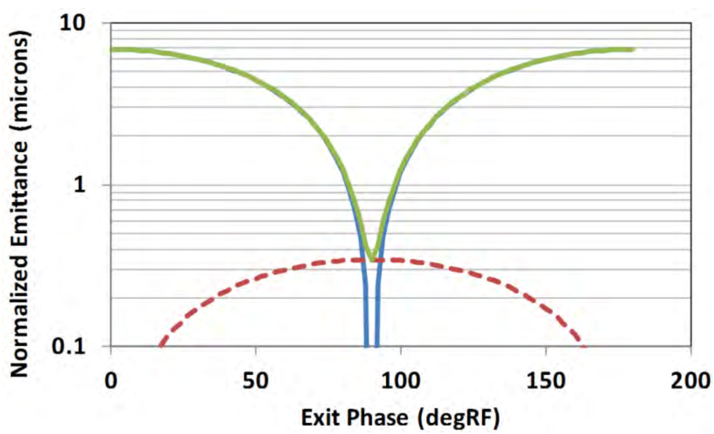

Figure 1.8. The RF emittance as a function of the exit phase for a 100 MV m^{-1} gun with a 1 mm rms size beam and a Gaussian longitudinal distribution of 4˚ rms at the exit iris. The total emittance (green solid) is the quadratic sum of the first-order (blue solid) and the second-order (red dash) emittances.

1.3.3. Longitudinal Beam Dynamics in the RF Field

Beginning with the force equations written in cylindrical coordinates, one can write the longitudinal force on an electron in a rotationally symmetric π-mode as

$$\frac{d}{dt}(\gamma m\dot{z}) = -eE_0\left[J_0(k_{01}r)\cos(k_z z)\sin(\omega t+\phi_0) - \frac{\omega\dot{r}}{k_{01}c^2}J_0'(k_{01}r)\cos(k_z z)\sin(\omega t+\phi_0)\right] \tag{1.29}$$

Expanding the Bessel functions and keeping the linear terms gives

$$\frac{d}{dt}(\gamma m\dot{z}) = -eE_0\left[\cos(k_z z)\sin(\omega t+\phi_0) + \frac{k_z r\dot{r}}{2c}\cos(k_z z)\cos(\omega t+\phi_0)\right] \tag{1.30}$$

In most cases, r/c is small and the second term can be ignored and we arrive at

$$\frac{\mathrm{d}}{\mathrm{d}t}(\gamma m\dot{z}) = -eE_0 \cos(k_z z)\sin(\omega t + \phi_0) \tag{1.31}$$

Kim emphasizes the importance of the backward-propagating wave in short linear accelerators such as RF guns. Since the field mode we're using is a standing wave mode, it naturally includes both forward and backward waves. It is easy to show that our equation for the longitudinal force agrees with Kim [1.18]. This is done by using a trigonometric identity to write Equ. 1.31 as

$$\frac{\mathrm{d}\gamma}{\mathrm{d}z} = -\alpha k_z\,[\sin(\phi)+\sin(\phi + 2k_z z)];\ \text{where } \alpha \equiv \frac{eE_0}{2mc^2 k_z} \tag{1.32}$$

Here, $\phi = \omega t - k_z z + \phi_0$ is the phase of the electrons with respect to the synchronous RF phase and we've defined the electric field parameter as α. This expression is identical to Equation 4 in Kim's paper [1.18].

The phase slip is computed from the following integral

$$\phi - \phi_0 = \omega t - k_z z = k_z \int_0^z \left(\frac{1}{\beta} - 1\right) dz \ = k_z \int_0^z \left(\frac{\gamma}{\sqrt{\gamma^2 - 1}} - 1\right) dz_0 \tag{1.33}$$

Since the beam is rapidly accelerated, the bunch quickly becomes relativistic and becomes synchronous with the RF fields and the phase slip becomes constant. Thus, the integrand is significant only near the cathode and the phase slip, ϕ rapidly approaches the asymptotic phase, ϕ_∞, given by [1.18]

$$\phi_\infty = \frac{1}{2\alpha \sin(\phi_0)} + \phi_0 \tag{1.34}$$

Bunch compression can be found by taking the derivative of the asymptotic phase with respect to the initial phase

$$\Delta\phi_\infty = \left[1 - \frac{\cos(\phi_0)}{2\alpha \sin^2(\phi_0)}\right]\Delta\phi_0 \tag{1.35}$$

Equ. 1.34 and Equ. 1.35 should be used with some caution. When Equ. 1.35 is negative, the bunch head and tail are reversed however simulations show this does not happen. Thus these expressions appear to be valid only for initial phases giving a positive result for the bunch compression. However, experiments and simulations do show that there is significant bunch compression for initial phases near the phase corresponding to zero field at the cathode. For example, in an S-band gun operating at 115 MV m^{-1}, a bunch with an initial phase of 30˚ S with respect to the zero field phase has the same length as the laser pulse. Initial phases less than 30˚ S can compress the bunch a factor of five or more at high cathode fields with an asymmetric bunch shape [1.21].

The electric field parameter and the initial phase establish the RF gun's operating range with respect to the RF emittance. Curves of constant electric field parameter, α, can be plotted in the plane formed by the asymptotic and initial phases as shown in Figure **1.9**. The figure shows the curves for electric field parameters, α = 0.5, 1.0.75, 1.0, 2.0 and 4.0. The asymptotic phase of 90˚ RF, where the RF emittance is a minimum, is shown by the horizontal dashed line. It can be seen that to reach the phase for minimum RF emittance requires $\alpha \approx 0.8$ or larger. In order for $\alpha > 1$ the product of the peak field and the RF wavelength needs to be greater than 6.4 MeV

$$eE_0\lambda_{RF} > 4\pi mc^2 \tag{1.36}$$

The peak field corresponding to $\alpha > 1$ is easily achieved for S-band (3 GHz, λ_{RF} = 10 cm) guns where the requirement is 64 MV m^{-1}. Typical S-band guns commonly operate at 100 MV m^{-1} and higher to give $\alpha > 1.5$. As the RF frequency increases, the field required for $\alpha = 1$ becomes more difficult. For example, the peak field needed at X-band (12 GHz) is 250 MV m^{-1}. This is possible, but on the high end of reliably achieved fields at this frequency. An X-band gun with a field of 200 MV m^{-1} has an electric field parameter of 0.8, which is too low to minimize the RF emittance as shown in Figure **1.9** for a 250 pC bunch charge and a cathode radius of 1 mm.

Of course, this restriction only applies to guns consisting of a string of iris coupled cavities and not to single cell guns. In addition, if the cavities are independently powered, they can be timed to give the desired exit phase at the expense of producing a mismatch of the focusing strength at the irises between the cells.

For initial phase near the RF zero crossing the RF field becomes equal to the bunch electric field and the space charge limit is reach. As will be discussed in the next section, the space charge field is related to the surface charge density, σ_{SCL}, and can be written as

$$\sigma_{SCL} = \frac{q_{bunch}}{\pi R_c^2} = \varepsilon_0 E_0 \sin(\phi_{0,SCL}) \tag{1.37}$$

$\phi_{0,SCL}$ is the initial phase at which the RF field equals the space charge field produced by a bunch charge with q_{bunch} and radius, R_c. Since $\alpha = \dfrac{eE_0}{2mc^2k_z}$, one can write

$$\alpha \sin(\phi_{0,SCL}) = \frac{eq_{bunch}}{2\pi\varepsilon_0 k_z R_c^2\, mc^2} \tag{1.38}$$

Thus bunches launched with an initial phase of $\phi_{0,SCL}$ and smaller are space charge limited and are not emitted. The space charge limited region is indicated by the shaded region in Figure **1.9** for a 250 pC bunch charge and a cathode radius of 1 mm.

The longitudinal emittance, ε_z, is defined in terms of the dimensionless longitudinal momentum, $p_z = \beta_z\gamma$, and the bunch length Δz

$$\varepsilon_z = \sqrt{\langle(\Delta p_z)^2\rangle\langle(\Delta z)^2\rangle - \langle\Delta p_z\rangle^2\langle\Delta z\rangle^2} = \sqrt{\langle[\Delta(\beta_z\gamma)]^2\rangle\langle(\Delta z)^2\rangle - \langle\Delta(\beta_z\gamma)\rangle^2\langle\Delta z\rangle^2} \tag{1.39}$$

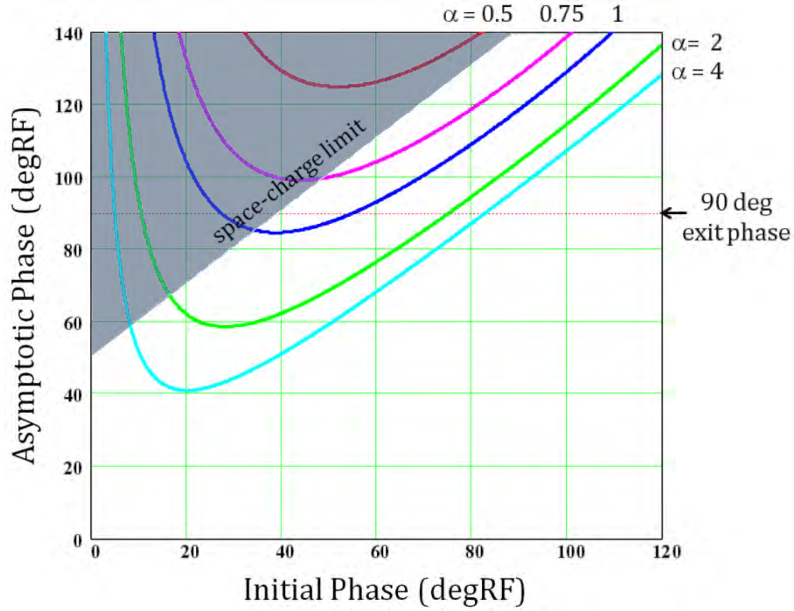

Figure 1.9. The asymptotic phase for an S-band gun plotted as a function of the initial phase for α = 0.5, 0.75, 1, 2 and 4. The region for which the cathode field is below the space charge limit is indicated in the upper left region of the graph. The space charge limit is shown for a 250 pC bunch with a 1 mm cathode radius.

The RF longitudinal emittance is derived from the beam energy for a small deviation $\Delta\phi$ from the mean phase, $\langle\phi\rangle$. For a Gaussian distribution and an on crest exit phase the longitudinal RF emittance is [1.18]

$$\varepsilon_z^{RF} = \sqrt{3}(\gamma_f - 1)k_z^2\,\sigma_z^3;\ \text{where } \langle\phi\rangle = 90^\circ\ \text{RF} \tag{1.40}$$

where γ_f is the final normalized energy of the beam. The longitudinal RF emittance is seen to have a cubic dependence upon the bunch length at an exit phase of 90˚ where the 1st-order transverse emittance is zero.

1.4 BEAM DYNAMICS WITH SPACE CHARGE

The beam charge from a cathode is limited in two operating regimes. For thermionic cathodes, there are two limits: Temperature limited emission and space charge limited emission. In temperature limited emission, the current density is given by the Richardson equation; the space charge limit of the current density is given by the Child-Langmuir law. In the case of photoemission, the bunch charge can be photon limited or space charge limited. The photon limited emission is given by the quantum efficiency (QE) times the number of incident photons, and space charge limited emission is given by a sheet beam model.

1.4.1 Space Charge Limited Emission

Electron emission is strongly affected by the electric field produced by the electron bunch itself. Immediately at the cathode surface, the electrons experience their own image charge, which for metal cathodes, produces a field opposing the applied electric field. The magnitude of this field is easily estimated by considering the electron bunch as a very thin charge sheet very close to the cathode surface, as shown in Figure **1.10**. In this case, the space charge field is similar to that between the plates of a capacitor, E_s.

In this case, the space charge field, E_{SCL}, is similar to that between the plates of a capacitor

$$E_{SCL} = \frac{q}{A\varepsilon_0} = \frac{\sigma}{\varepsilon_0} \tag{1.41}$$

where A is the cross-sectional area of the sheet beam, q is the residual charge, and ε_0 is the permeability of free space. Electron emission saturates when $E_{SCL} = E_{applied}$, whether $E_{applied}$ is an RF or DC electric field

$$E_{SCL} = \frac{q}{A\varepsilon_0} = \frac{\sigma}{\varepsilon_0} = E_{applied} \tag{1.42}$$

Thus, for a RF photocathode gun, the bunch surface charge density is limited when

$$\sigma_{SCL} = \varepsilon_0 E_0 \sin(\phi_0) \tag{1.43}$$

Here, E_0 is the peak RF field on the cathode and ϕ_0 is the laser launch phase.

At the space charge limit (SCL), the emitted charge saturates and the emission becomes constant. If the transverse distribution is non-uniform when the cathode is driven to the SCL, then different locations will saturate and other areas will not. In the RF gun, the signature observation of the SCL is the sub-linear dependence of the charge on the laser energy as shown in Figure **1.11**.

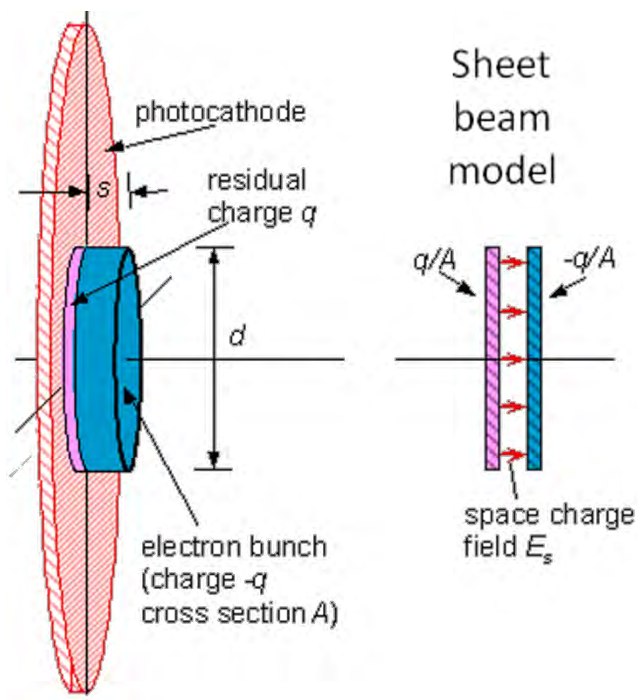

Figure 1.10. Sheet beam model for short pulse photoemission. [Courtesy of A. Vetter]

The space charge limit of the surface charge density in an RF gun is linear with the applied field. This differs from the 3/2-power for the voltage given by the Child-Langmuir law for surface current density, J_{CL}, thermionic emission [1.22]

$$J_{CL} = 1.67\times10^{-3}\sqrt{\frac{e}{mc^2}}\frac{V^{3/2}}{d^2} \tag{1.44}$$

J_{CL} is the space charge limited current surface density of beam filling a cathode-anode gap as shown in Figure **1.12**. The voltage across the gap is V and the gap length is d.

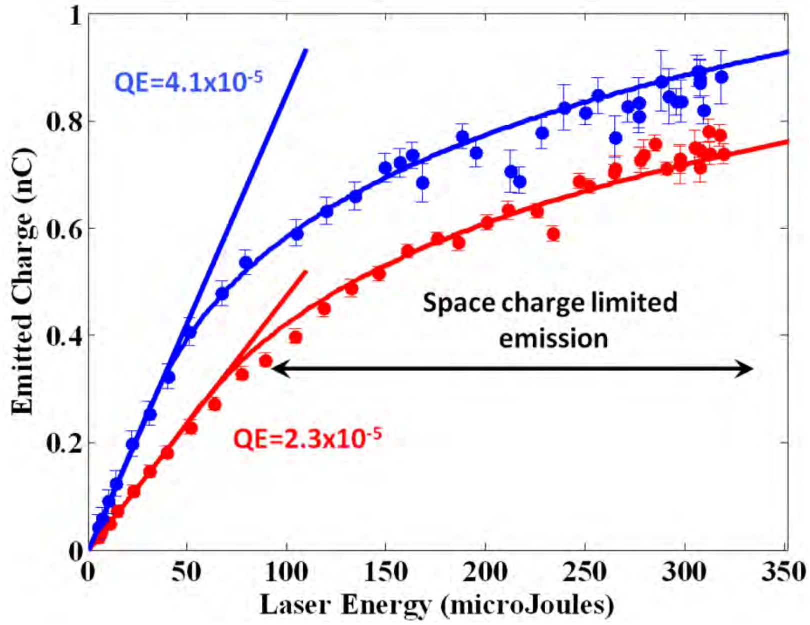

Figure 1.11. The measured bunch charge vs. laser energy fit with an analysis for the QE and the SCL.

Equ. 1.43 and Equ. 1.44 show the space charge limits are different for short and long electron bunches. Equ. 1.43 is derived assuming planar cathode and anode electrodes with a potential difference V and a gap separation d with a continuous stream of electrons between the electrodes. Thus, the SCL is linear with the electric field for a sheet-like beam, while the surface current density has a 3/2-power voltage dependence for a continuous beam in a planar diode.

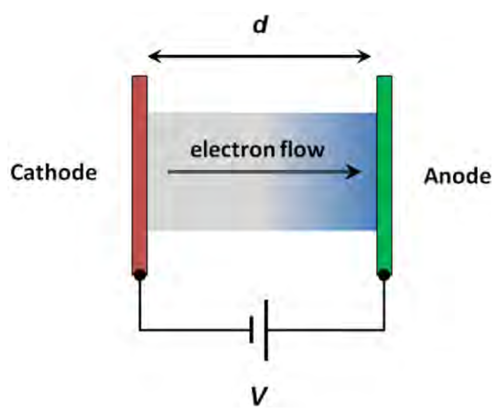

Figure 1.12. Electron current in the diode region of a thermionic or long pulse gun.

One computes the emitted charge as a function of the laser pulse energy by applying the simple assumption that emission saturates at the SCL. The emitted bunch charge as a function of the incident laser pulse energy is separated into two regions. For low laser energies below the SCL, the curve is linear with a slope related to the quantum efficiency, QE,

$$q_{bunch} = \frac{eE_{laser}}{\hbar\omega}\,\mathrm{QE} \tag{1.45}$$

where q_{bunch} is the emitted bunch charge, E_{laser} is the laser pulse energy and $\hbar\omega$ is the laser photon energy. Let us assume a Gaussian for the transverse distribution of the laser with σ_r for the rms width of the

Gaussian. Then when the laser pulse energy is high enough for the peak of the Gaussian to produce a surface charge density equal to the applied field and the SCL is reached. At the SCL, the bunch charge saturates or no longer increases with increasing laser pulse energy.

The situation is shown in Figure **1.13**, where the full Gaussian distribution (red line) is truncated to the SCL in its core (green dark). The total charge then, $q_{emitted}$, consists of the core, q_{core}, charge plus the charge emitted in the unsaturated tails, q_{tail} [1.23]

$$q_{emitted} = q_{core} + q_{tail} \tag{1.46}$$

Radial integration of the core and tail regions of the transverse distribution gives the space charge limited bunch charge as

$$q_{emitted} = \pi r_m^2 \varepsilon_0 E_0 \sin(\phi_0) + \mathrm{QE}\,\frac{eE_{laser}}{\hbar\omega}\exp\left(\frac{-r_m^2}{2\sigma_r^2}\right) \tag{1.47}$$

with the radius of the saturated core, r_m, given by

$$r_m = \sigma_r\sqrt{2\ln\left(\frac{eE_{laser}\mathrm{QE}}{2\pi\varepsilon_0\sigma_r^2\hbar\omega E_0\sin(\phi_0)}\right)} \tag{1.48}$$

These expressions can be used to fit the charge vs. laser energy data such as shown in Figure **1.13**, to obtain the QE from the linear portion, as well as the rms radius of the equivalent Gaussian distribution. It also can crudely verify the strength of the electric field on the cathode when a direct measurement of the beam energy isn't possible.

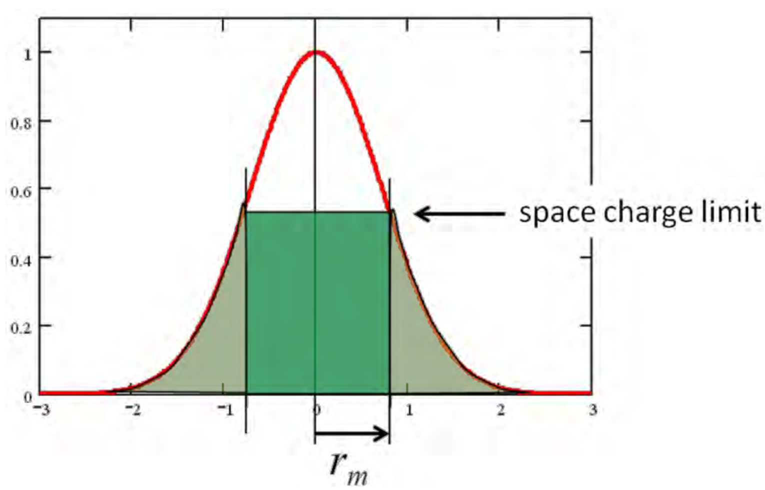

Figure 1.13. The radial Gaussian distribution (red solid) showing the space charge limited core (green dark) and emission from the tails (green light).

1.4.2 Space Charge Emittance due to the Bunch Shape

Using two models, we discuss the emittance growth due to the transverse space charge forces which can be separated into two spatial scales. The first, on the scale of the beam size, is due to the overall radial expansion of the bunch shape. It is dependent upon the transverse- to longitudinal-aspect ratio and the functional form of the charge distribution, for example, whether the bunch distribution is Gaussian or cylindrical. The second space charge emittance source occurs on a much shorter length scale during the homogenizing or smoothing of the transverse charge density during initial acceleration near the cathode.

In Kim's theory, both the transverse and longitudinal the space charge emittance is given as [1.18]

$$\varepsilon_i^{SC} = \frac{\pi}{4}\frac{1}{\alpha k_z \sin(\phi_0)}\frac{I}{I_0}\mu_i(A);\ \text{where } i = x \text{ or } z \tag{1.49}$$

where I is the peak current at the bunch center and I_0 is the characteristic current of 17 kA. (Note: The critical current or Alfven current is energy dependent, $I_A = \beta\gamma I_0$.) The transverse- and longitudinal-space charge factors, $\mu_i(A)$, are the square root of the variance of the normalized transverse and longitudinal fields, respectively, in terms of the bunch aspect ratio, A.

For a rotationally symmetric, transverse and longitudinal Gaussian distribution with respective rms sizes of σ_x and σ_z, the aspect ratio is

$$A_{gaussian} = \frac{\sigma_x}{\sigma_z} \tag{1.50}$$

To an excellent approximation, the space charge factors can be parameterized as

$$\mu_x^{gaussian}(A) = \frac{1}{3A + 5} \tag{1.51}$$

and

$$\mu_z^{gaussian}(A) = \frac{1.1}{1 + 4.5A + 2.9A^2} \tag{1.52}$$

In the case of a uniformly charged cylindrical volume of radius a and length L, the aspect ratio is

$$A_{cylinder} = \frac{a}{L} \tag{1.53}$$

A cylinder's transverse factor is accurately described by

$$\mu_x^{cylinder}(A) = \frac{1}{35\sqrt{A}} \tag{1.54}$$

Returning to Equ. 1.49, the emittance equation, it can be seen that for a constant peak current, the bunch shape's effect on the space charge emittance is entirely contained in the space charge factor. In Figure **1.14**, we plot the Gaussian and cylindrical transverse space charge factors as a function of the aspect ratio and observe that the space charge factor of a uniformly charged cylinder is four or more times lower than for a Gaussian. The longitudinal space charge factor for a cylinder is approximately an order-of-magnitude smaller than the Gaussian longitudinal factor. This is the theoretical motivation behind needing a uniform laser pulse to produce low emittance beams.

The decline of transverse factors with increasing aspect ratio is shown for both bunch shapes, showing that the "pancake-like," $A > 1$, bunch has much lower space charge emittance than do "cigar-like" shapes, $A < 1$. Thus, the conclusions are the shorter the bunch the better and the shape should be a uniformly charged cylinder.

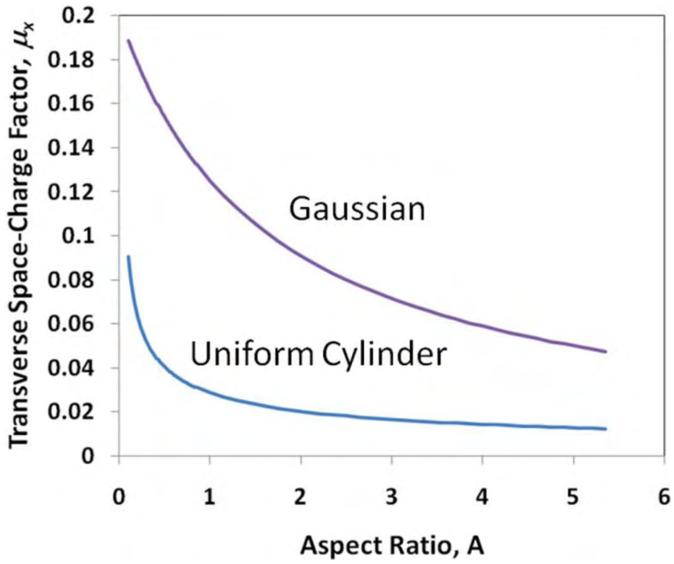

Figure 1.14. The space charge factors for Gaussian and cylindrical bunch shapes.

1.4.3 Space Charge Emittance due to Non-uniform Transverse Emission

A high spatial frequency intensity modulation across the emission area is a second general type of non-uniformity which is another important source of space charge emittance.

Experimental and theoretical studies have quantified the effect of non-uniform emission upon beam quality for space charge dominated beams [1.24], [1.25]. This work was done to establish the uniformity required to achieve low emittance beams for short wavelength FELs. Recent experiments performed at the SLAC LCLS FEL measured the effect emission uniformity has upon emittance and lasing at X-ray wavelengths. In this work, a space charge model has been developed which agrees well with emittance measurements for various mesh patterns of the drive laser projected onto the cathode [1.26]. Here, the model is formulated in terms of the spatial frequency of the non-uniform emission.

The beamlet space charge model is for a beam with overall radius R composed of a large number of smaller beamlets arranged in a rectangular transverse pattern. Assume each beamlet has an initial radius r_0 and center to center spacing of $4r_0$ in a rectangular grid, as shown to the left in Figure **1.15**. Internal transverse space charge forces make each beamlet expand and merge with its neighboring beamlets, as illustrated in Figure **1.15** (right). This radial acceleration gives the beamlets transverse momentum leading to larger emittance for the total beam.

The radial expansion ends when the beamlets merge and form an approximately uniform distribution. At this point, the non-uniformity space charge emittance becomes constant. Simulations and analytic modeling of this geometry show the beamlets overlap within tens of picoseconds, therefore the non-uniformity emittance is generated very close to the cathode before the beam can become relativistic for even the very highest cathode RF fields. It is interesting to note that the electrons are still non-relativistic and the beamlets are merging at the head of each bunch, even while the tail electrons are just leaving the cathode.

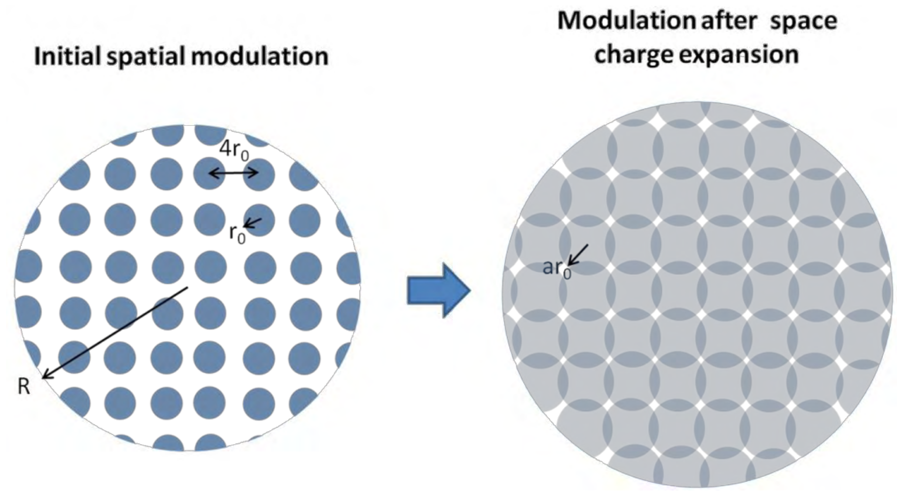

Figure 1.15. Modulation patterns used to compute the space charge emittance. Left: The initial pattern on the cathode consisting of a rectangular array of circles with radius r_0 and a spacing of $4r_0$ within a full beam radius R. Right: Schematic view of the beamlet pattern after expansion due to transverse space charge forces. The integration of the transverse force ends when the beamlets with radius ar_0 begin to overlap and form a quasi-uniform distribution.

The space charge emittance for the pattern shown in Figure **1.15** with a 100% depth of modulation in terms of the beam radius, R, the radius of a beamlet, r_0, and bunch peak current, I, is

$$\varepsilon_{n,sc} = \sigma_x \frac{4r_0}{\sqrt{\pi}R}\sqrt{\frac{I}{I_0}} \tag{1.55}$$

The characteristic current is $I_0 = ec\, r_e^{-1} \approx 17$ kA, where r_e is the classical radius of the electron. The $\sqrt{I}$ dependence is similar to that found previously by Wangler [1.27]. In his theory, the space charge emittance grows linearly with beam position z until the beam has travelled a quarter of a plasma period. At this point, the emittance "saturates" to an approximately constant value. In the beamlet model, the emittance saturates when the beamlets overlap and there's no charge gradient driving the transverse acceleration of the electrons.

It is useful to write the emittance in terms of the beamlet spatial number, or the number of beamlets, n_s, across the beam diameter, $2R$. Since the beamlet spacing is $4r_0$, n_s is

$$n_s = \frac{R}{2r_0} \tag{1.56}$$

Therefore, the space charge emittance due to this transverse expansion immediately after emission can then be written as

$$\varepsilon_{n,s}(n_s,I) = \sigma_x \frac{2}{\sqrt{\pi n_s}}\sqrt{\frac{I}{I_0}} \tag{1.57}$$

Thus, the emittance decreases as the distance between the beamlets decreases or their spatial number increases. This clearly is because the shorter the expansion distance over which the beamlets can expand and undergo transverse acceleration, the smaller the final transverse velocity, and hence the smaller the emittance. Figure **1.16** shows the normalized divergence as a function of the spatial number for peak currents of 100 A, 40 A and 10 A which for LCLS parameters approximately corresponds to 1 nC, 250 pC and 20 pC bunch charge. This model is in reasonably good agreement with experimental results [1.26].

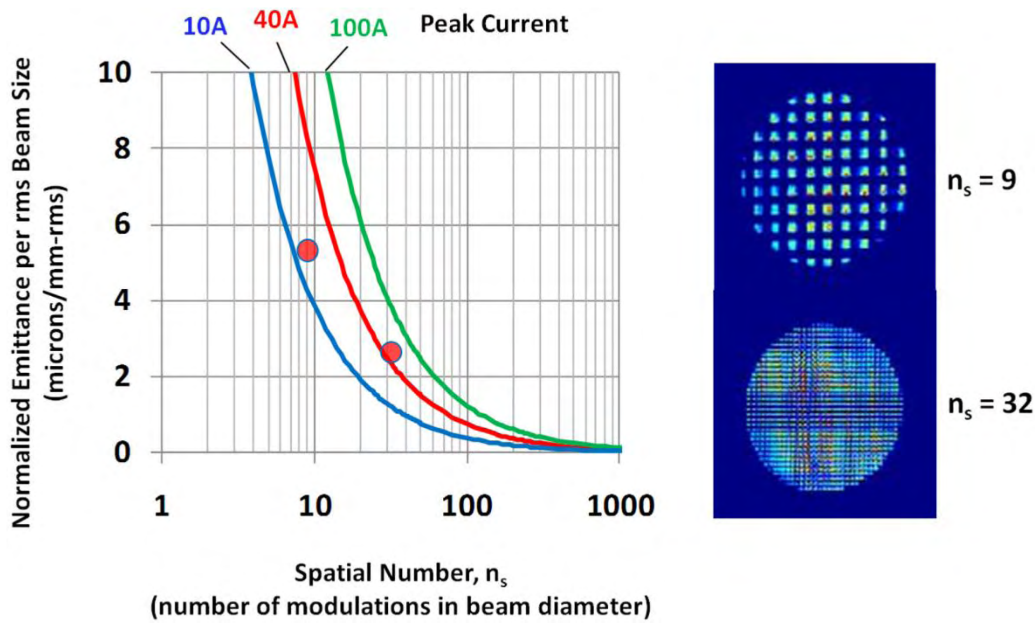

Figure 1.16. The normalized divergence due to transverse space charge forces of a patterned emission distribution as a function of the number of modulations or beamlets across the beam diameter. Curves are shown for peak currents of 10 A (red), 40 A (blue) and 100 A (green). The red points are measured projected emittances, from which the uniform beam emittance has been subtracted in quadrature and then divided by the rms size of the laser spot to give the experimental normalized divergence. The right images are the laser patterns used to produce the experimental emittance shown by the respective points on left graph, modulation numbers 9 and 32. [[1.26]; Adapted under Creative Common Attribution 3.0 License (www.creativecommons.org/licenses/by/3.0/us/) at www.JACoW.org.]

The thoughtful reader may notice that there is no energy dependence or cathode field strength in Equ. 1.57; this may seem wrong since it is generally assumed that the space charge force is mitigated by the rapid acceleration of the beam, and so any formulation of the space charge emittance should include the accelerating electric field or beam energy. However, this model assumes the emittance growth occurs before the beam can reach a relativistic energy. Therefore, there is no dependence upon the cathode field and this emittance is only reduced by making the emission uniform.

1.4.4 Emittance Compensation Theory

Emittance compensation in an RF gun was first explained by Carlsten [1.28] who used the concepts of slice and projected emittances to show how the projected emittance could be reduced by aligning the short longitudinal slices in transverse phase space. Emittance compensation theory divides the electron bunch into thin temporal slices and assumes they are not mutually interacting. Each slice's emittance is assumed to be the same, small (except in the presence of geometric aberrations), and nearly equal to the thermal emittance. Their relative orientation in transverse phase space differs from slice to slice, *i.e.*, the slices all have different Courant-Snyder parameters and betatron functions. Most analyses, such as the one presented here, assume the slice emittance and phase space parameters vary slowly along the bunch and that a constant peak current can be used for all bunches. An example of a configuration of slices with their phase spaces rotated along the bunch is shown in Figure **1.17**. While the emittance of each slice is quite small, the projected emittance of an ellipse enclosing all the slices is much larger. Aligning the slices in transverse phase space gives projected emittance which approaches the emittance of a single slice. However, it is typically larger depending upon the relative orientation of the slices in phase space.

The concept of emittance compensation is shown graphically in Figure **1.18**. At the cathode all the slices from the bunch head (green) to the bunch tail (red) are born with very low divergence over the size of the emission area (Figure **1.18(a)**). The projected emittance is nearly the same as the intrinsic emittance. As the beam expands from the cathode, the space charge forces give the head and tail different kicks in transverse angle depending upon the peak current of the bunch as shown in more detail below. This increases the projected emittance shown as the area enclosed by the ellipse as shown in Figure **1.18(b)**. Uncorrected, this emittance would persist and grow as the beam propagates down the beam line. However, a solenoid can recover the low emittance. Figure **1.18(c)** shows the angle kick given to the beam by the solenoid lens which gives the bunch head, middle and tail the same sign for the divergence. The beam now drifts a distance with the slices all converging at a beam waist (Figure **1.18(d)**).

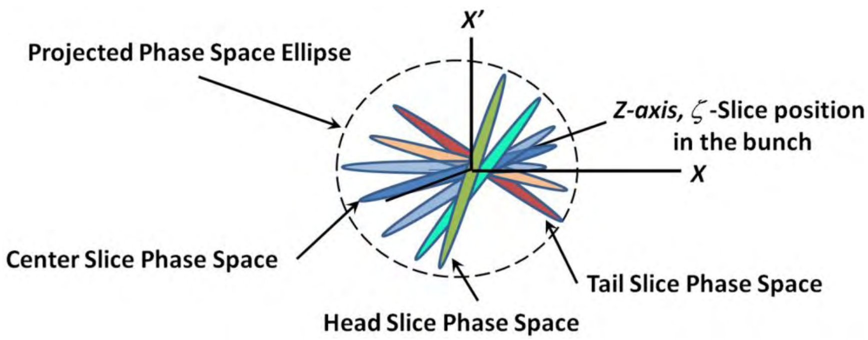

Figure 1.17. Dividing the bunch longitudinally to form thin slices each with its own phase space distribution. The slice phase spaces are assumed to be independent and do not interact between themselves. The projected emittance is the phase space ellipse which encloses all the slice phase spaces.

The beam waist is located at the entrance to the high-energy linac which rapidly accelerates the beam to relativistic energy from the space charge dominated to emittance dominated regimes. This beam optics is essentially producing a parallel-to-point image of the beam from the cathode to the linac. As long as the space charge force is linear, its kicks can occur anywhere along the beam line and still be corrected with a linear solenoid lens. The linearity of the space charge forces is a key ingredient in the emittance compensation technique along with proper matching of the bunch slices into the high energy accelerator to freeze the aligned slices.

Emittance compensation was first described by Carlsten [1.28] to explain simulations showing the projected emittance oscillating along the beamline. This theory was later expanded upon by Serafini and Rosenzweig who showed the oscillation period is related to the bunch plasma frequency, and that there is a preferred matching of the beam size and divergence to the beam line optics (called the invariant envelope) which minimizes the emittance [1.29]. Later work by Ferrario *et al.* showed there is an optimum beam size and divergence at the entrance to the first linac which minimizes the space charge emittance [1.30] and measured the emittance oscillations, thereby verifying the theory [1.31].

The Serafini and Rosenzweig formalism is based on balancing the space charge defocusing of the beam with an applied focusing force. The result is a beam whose radius and emittance oscillates with the bunch plasma frequency. In their analysis, the space charge kick shown in Figure **1.18(b)** is applied continuously along a channel of radial focusing fields. The outward radial space charge force is balanced by the focusing fields. If the space charge and focusing fields are linear, then the beam is transported without emittance growth. However, for most beam distributions, the space charge force is not linear leaving some emittance uncompensated for given the linear focusing fields.

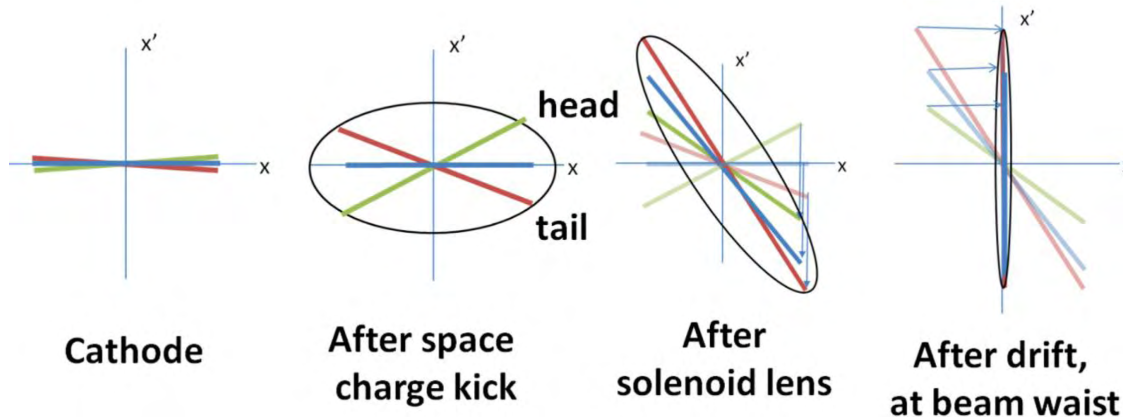

Figure 1.18. Transverse phase space dynamics during emittance compensation. The transverse phase space is shown for different slices along the bunch. The bunch head slice is shown as a green line, the tail slice is red and the center slice is blue. An ellipse has been drawn around the three slices to indicate the projected phase space of the three slices.

Compensation of the space charge force is best computed by beginning with the beam envelope equation for a slice with current $I(\zeta)$ in a uniform focusing channel

$$\sigma_r''(\zeta) + K_r\sigma_r(\zeta) = \frac{I(\zeta)}{2I_0(\beta\gamma)^3\sigma_r(\zeta)} + \frac{\varepsilon^2_{n,intrinsic}(\zeta)}{(\beta\gamma)^2\sigma_r^3(\zeta)} \tag{1.58}$$

where $\sigma_r(\zeta)$ is the rms radial beam size for a slice at position ζ, K_r is the channel focusing strength, $\varepsilon_{n,intrinsic}$ is normalized intrinsic emittance of the cathode, and I_0 is the characteristic current given by $I_0 = 4\pi\varepsilon_0 mc^3\, e^{-1}$, which again is 17 kA for electrons. The intrinsic (a.k.a. thermal) emittance is also allowed to be different for different slices. The slice each is $\delta\zeta$ long at position ζ along the bunch as shown in the Figure **1.19(a)**. β is the electron velocity in units of c and γ is the total energy normalized to the electron rest mass, mc^2.

The envelope equation given in Equ. 1.58 implies there is no transverse offset of the slice centroids with respect to each other. Including this in the calculation requires using the ray equation to take into account the relative displacement of position and angle between each slice. Although this aspect of the topic is not pursued any further in this chapter, it can be a significant effect in systems with unbalanced RF feeds, *etc.* [1.32].

Each slice can be characterized by its divergence and beam size in transverse phase space and current, as shown in Figure **1.19**. The slice current and slice radius determine the defocusing strength of the space charge field. The slices can have different sizes, divergences as well as different correlations between the size and divergence, as shown in Figure **1.19(b)**.

For a space charge dominated beam, the emittance term is small compared to the current term and the emittance dependence can be ignored. In balanced flow the space charge defocusing is exactly counteracted by the external focusing field with focusing strength K_r. In this case the beam drifts with laminar flow in which the electron trajectories do not cross. This balance between the radial space charge defocusing and external focusing is called Brillouin flow. [1.33] A beam in Brillouin flow has a static envelope equation for a given equilibrium beam size of a slice, σ_{eq}

$$\sigma'' = -K_r\sigma_{eq} + \frac{I}{2I_0(\beta\gamma)^3\sigma_{eq}} = 0 \tag{1.59}$$

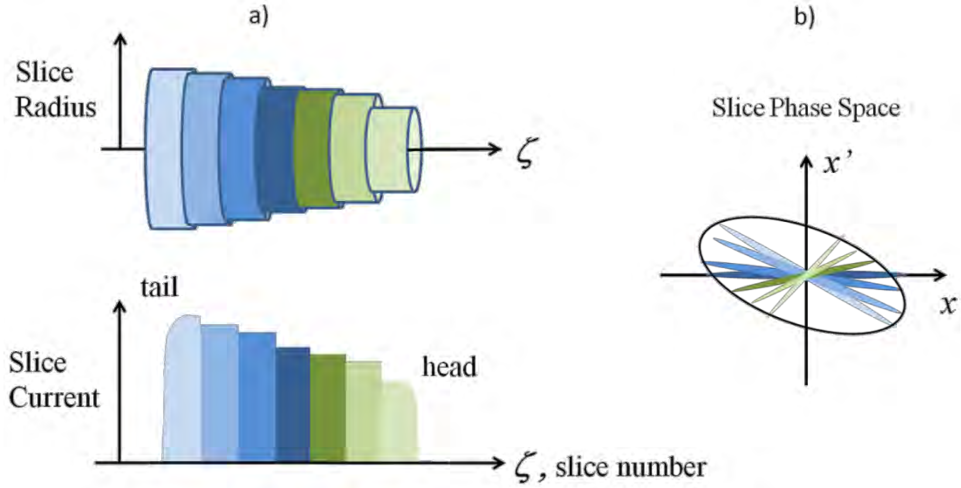

Figure 1.19. a) The bunch is modeled by dividing it into thin sections or slices along the bunch ζ-axis. Each slice is $\delta\zeta$ long. Simulations show that dividing the bunch into 10 or more slices accurately represents the beam dynamics. b) The areas and orientations of the slices in transverse phase space.

Here, K_r is the external radial focusing strength which balances the space charge force for an equilibrium rms beam size for each slice

$$\sigma_{eq}(\zeta) = \sqrt{\frac{I(\zeta)}{2I_0(\beta\gamma)^3 K_r}} \tag{1.60}$$

Since K_r is the same for all slices, the only thing causing the equilibrium size to vary between slices is the slice current. Variations in the slice current correspond to different equilibrium sizes. This deviation of the actual size from the equilibrium size increases the projected emittance due to their different orientations of the slice in phase space as shown in Figure **1.19(b)**.

To derive the projected emittance consider a small change or perturbation in the slice radius away from the equilibrium radius

$$\sigma(\zeta) = \sigma_{eq}(\zeta) + \delta\sigma(\zeta) \tag{1.61}$$

Inserting this small deviation into the envelope equation for balanced flow and keeping the lowest order term in $\delta\sigma(\zeta)$ gives

$$\delta\sigma''(\zeta) + 2K_r\delta\sigma(\zeta) = 0 \tag{1.62}$$

The solution for this equation is the sum of sine and cosine functions times the initial (*i.e.*, at $z = 0$) slice deviation of size and divergence, respectively. The size oscillation of each slice as a function of distance along the channel is then

$$\delta\sigma(z,\zeta) = \frac{\delta\sigma_0'(\zeta)}{\sqrt{2K_r}}\sin\left(\sqrt{2K_r}\,z\right) + \delta\sigma_0(\zeta)\cos\left(\sqrt{2K_r}\,z\right) \tag{1.63}$$

As a reminder, K_r is the external radial focusing strength and z is the distance the bunch has traveled along the beamline.

To compute the emittance we assume that all the slices are identical except for their current. Specifically, all the slices initially have the same size, σ_0, and zero divergence variation at z = 0. Then, each slice's initial deviation from the equilibrium size is related to the slice current

$$\delta\sigma_0(\zeta) = \sigma_0 - \sigma_{eq}(\zeta) = \sigma_0 - \sqrt{\frac{I(\zeta)}{2I_0(\beta\gamma)^3 K_r}} \tag{1.64}$$

With these initial conditions, each slice undergoes a small size oscillation about the equilibrium beam size, σ_{eq}, as it propagates along the focusing channel

$$\sigma(z,\zeta) = \sigma_{eq}(\zeta) + [\sigma_0 - \sigma_{eq}(\zeta)]\cos\left(\sqrt{2K_r}\, z\right) \tag{1.65}$$

The projected emittance is proportional to the rms of the slice currents normalized to the bunch peak current, I_p, and is given as

$$\varepsilon_{n,comp}(z) = \frac{1}{2}\sqrt{K_r}\sigma_0\sigma_{eq}(I_p)\frac{\delta I_{rms}}{I_p}\left|\sin\left(\sqrt{2K_r}\, z\right)\right| \tag{1.66}$$

Where δI_{rms} is the rms current computed from the distribution of the slice currents. The projected emittance thus oscillates with the same wave number as does the beam size, but is shifted $\pi/2$ in phase [1.29].

It is useful to make some further simplifying assumptions to the compensation emittance. For instance, since the size deviation is small, the initial slice size is approximately equal to the equilibrium size. Therefore, Equ. 1.66 reduces to

$$\varepsilon_{n,comp}(z) = \frac{\delta I_{rms}}{\sqrt{2K_r}\, I_0\, (\beta\gamma)^3}\left|\sin\left(\sqrt{2K_r}\, z\right)\right| \tag{1.67}$$

It is interesting to consider the emittance as $\left(\sqrt{2K_r}z\right)$ becomes small and goes to zero. This is useful for estimating this projected emittance close to the cathode or in very weak focusing channels. As $\left(\sqrt{2K_r}z\right) \rightarrow 0$, the emittance further simplifies to

$$\varepsilon_{n,comp}(z) \propto \frac{\delta I_{rms}}{\sqrt{2K_r}I_0(\beta\gamma)^3}\, z;\ \text{where}\ \left(\sqrt{2K_r}z\right) \propto 1 \tag{1.68}$$

Therefore, solutions of the balanced envelope equation show an oscillating projected emittance as a function of z. The slice radii oscillate for small deviations from the balanced beam envelope. The solutions show all the slice envelopes oscillate about the balanced envelope with the same z-coordinate wave number, $\sqrt{2K_{r,eq}}$, and the amplitude results from the initial deviation in the beam size from equilibrium size. If the slices are aligned in transverse phase space at one z-position, then there are periodic locations where the slices re-align and the projected emittance is a local minimum. This occurs irrespective of the initial slice amplitude. Optimal compensation of the linear space charge emittance due to different slice currents occurs at these local minima.

Thus, in addition to compensating for the projected emittance due to misaligned slices, it is also necessary to match the beam into a high gradient booster accelerator and damp the envelope oscillations to a low emittance. The required matching condition is referred to as the Ferrario working point [1.30], formulated for the LCLS injector. In this scheme, the RF focusing of the linac is matched to the invariant envelope to damp the emittance to its final value at a relativistic energy. The working point matching condition requires the emittance to be a local maximum and the envelope to be at a waist at the entrance to the booster. The waist size is determined by the strength of the RF fields. RF focusing provides a weak focusing channel and acceleration damps the emittance oscillations.

Matching the beam to the first accelerator needs to be included as part of emittance compensation and should obey the following basic conditions at the entrance to the linac: the beam is at a waist: $\sigma' = 0$ and the waist size at injection is determined by a balancing of the RF transverse force with the space charge force. The second requirement establishes balanced flow similar to that used in emittance compensation.

As an example, assume the RF lens at the entrance to the booster is similar to the RF kick given at the gun exit (see Section 1.2). Assume the beam is injected into the linac on the crest of the RF waveform for maximum acceleration. In this case, the RF lens deflection is

$$\sigma'_{linac} = \sigma_{linac} \frac{eE_{linac}}{2\gamma mc^2} \tag{1.69}$$

where σ_{linac} is the rms transverse beam size at the entrance of the linac, E_{linac} is the linac peak accelerating field, and γmc^2 is the total beam energy. Taking the derivative gives the RF force

$$\sigma'' = -\sigma_{linac} \frac{eE_{linac}}{2\gamma^2 mc^2} \gamma' = -\sigma_{linac} \frac{\gamma'^2}{2\gamma^2} \tag{1.70}$$

since $\gamma' = \frac{eE_{linac}}{mc^2}$. The envelope equation for the matched beam is then

$$\sigma'' = -\sigma_{match} \frac{\gamma'^2}{\gamma^2} + \frac{\mathrm{I}}{2I_A \gamma^3 \sigma_{match}} = 0 \tag{1.71}$$

and solving for the matched beam size gives

$$\sigma_{matched} = \frac{1}{\gamma'} \sqrt{\frac{I}{2I_A \gamma}} \tag{1.72}$$

as the waist size at injection into the linac. Once matched the beam emittance decreases along the accelerator due the initial focus at the entrance and Landau damping. This behavior has been verified using HOMDYN, an envelope code using slices, and the particle-pusher code, PARMELA. These codes are described in Section 1.7.

It is relevant to note that this technique of emittance compensation makes no assumption about the nature of the focusing channel. Therefore, this analysis applies equally well to both RF and DC guns. In fact, the same fundamental concept has been applied to the merger optics of a space charge dominated beams into energy recover linacs, as well as other beam transport systems.

1.5 GUN-SOLENOID OPTICS AND OPTICAL ABERRATIONS

The strong defocusing at the gun exit requires compensation by an equally strong focusing lens. The focusing is usually provided by a solenoid with a longitudinal magnetic field. It is relevant to comment on the dual role of the solenoid; it not only cancels the strong negative RF lens, but it also plays a crucial function of emittance compensation by aligning the slices transversely along the bunch to minimize the projected emittance.

This section begins with the description of a first-order model of the gun and solenoid system. This model is used to illustrate how the cathode uniformity of emission can be imaged when the solenoid is adjusted to image electrons from the cathode on a view screen. Section 1.5.2 presents a derivation of the first-order chromatic aberration of the solenoid. Section 1.5.3 shows simulation results for the geometric aberrations of the solenoid and the Section 1.5.4 discusses quadrupole field errors of the solenoid. It is shown that the emittance due to quadrupole field errors can be fully recovered with correction quadrupoles.

1.5.1 First-order Optics Model of the Gun

The RF gun can be assumed to be a series of thin lenses positioned at the entrance and exit of each cavity for an electron-RF phase which accelerates the beam. If the fields in each cavity are balanced, then the defocus at the exit of one cavity is cancelled by the focus of the next cavity. This is approximately true for all the internal cavities of the gun or any acceleration section. However, there is no cancellation of the defocus at the exit of the last cavity, which as shown in Section 1.3.2 results in linear and non-linear RF projected emittance. For a beam exit phase of 90˚ then the linear RF emittance is zero leaving only the second-order emittance (see Figure **1.8**). However, Figure **1.7** shows that while the emittance is minimal at 90˚, the RF strongly defocuses the beam, requiring an equally strong focusing provided by the gun solenoid. As noted in the discussion after Equ. 1.22, the focal length of the RF gun is 12 cm for an exit energy of 6 MeV and a peak field of 100 MV m^{-1}.

$$f_{RF} = \frac{-2\gamma mc^2}{eE_0 \sin(\phi_0)} \tag{1.73}$$

Equ. 1.73 is the same as Equ. 1.22, however, β is considered to be unity at these energies. Due to the strong defocusing of the RF gun it is necessary to use a comparably strong focusing lens to collimate and match the beam into the high energy booster linac. If this focusing is done with a solenoid, then its focal strength, K, in the rotating frame of the electrons, f_{sol}, is [1.34]

$$\frac{1}{f_{sol}} = K \sin(KL_{sol}); \text{ where } K \equiv \frac{B(0)}{2(B\rho)_0} = \frac{eB(0)}{2p} \tag{1.74}$$

where $B(0)$ is the field of the solenoid, L_{sol} is the solenoid effective length, $(B\rho)_0$ is the magnetic rigidity, and p is the beam momentum with units of [GeV c^{-1}]. The rigidity can be expressed in the following useful units as

$$(B\rho)_0 = \frac{p}{e} = 33.356p \text{ [kG m]} \tag{1.75}$$

With the assumption that the focusing effects of adjacent cavities cancel, the first-order optics of the gun and solenoid can be modeled with a single thin defocusing lens for the RF and a thick solenoid. Besides using the solenoid to cancel the RF defocusing and for space charge emittance compensation, it is also useful for imaging the electron emission from the cathode with the configuration shown in Figure **1.20**.

The transformation of beam rays from the cathode to the view screen can be computed using linear matrix algebra of ray optics. With simple matrix multiplication, electrons emanating from the cathode with position and angle displacements relative to a central ray can be computed to the view screen.

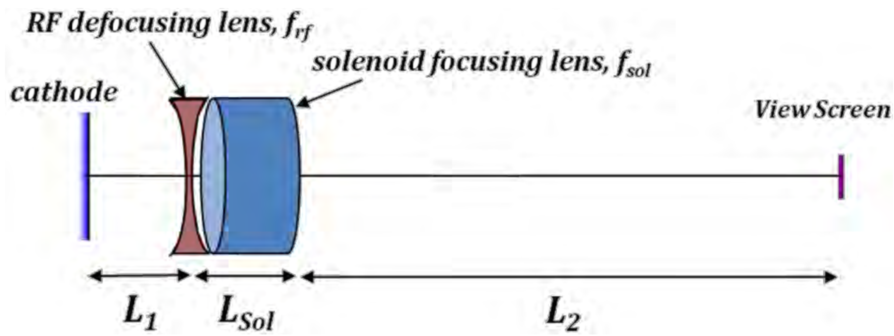

Figure 1.20. Configuration of a first-order optical model showing principal optical elements of the gun, solenoid and drift distance to a view screen, which can be used to compute the cathode emission onto a view screen. For the LCLS S-band gun-to-linac region: L_{sol} = 19.35 cm, L_1 = 12.3 cm and L_2 = 106.6 cm, which gives a magnification of approximately -3.6 for a point-to-point image.

The calculation for the optical system when the solenoid is adjusted to form an image (point-to-point imaging) of the cathode emission on the view screen gives the magnification, M, as

$$M = \cos(KL_{sol}) - L_2 K \sin(KL_{sol}) - \frac{1}{f_{RF}}\left(\frac{\sin(KL_{sol})}{K} + L_2 \cos(KL_{sol})\right) \tag{1.76}$$

The magnification depends upon the solenoid and gun field parameters and not upon the distance to the cathode. The magnification is easily measured by inserting a target of known size into the laser beam optics at the object plane, which is then imaged onto the cathode. The size of this target is then measured on the view screen when an image is formed using the solenoid. A magnification of 3-4 is typical in S-band guns.

Electron beam images on a YAG view screen of a 6 MeV beam from an S-band gun with a peak cathode field of 115 MV m^{-1} is shown in Figure **1.21**. The view screen images where taken using the second YAG screen shown in Figure **2.21**. The solenoid has been adjusted to produce an image of the emission pattern at the YAG's position. The electron magnification for the imaging from the cathode to the YAG screen is -3.6 in agreement with Equ. 1.76. The emission is the 2-D product of the QE and laser distributions. In these measurements, the laser distribution is known to have good uniformity and vary slowly over its diameter (low spatial frequencies); therefore, the observed images are good representations of the true QE map.

The two images in Figure **1.21** show very different emission patterns for the same cathode at different times in its two years of operation in the S-band gun. The image in Figure **1.21(a)** shows the QE map consists of small hot spots. These hot spots were observed for low QE, in the range of 10^{-6}. The emission image in Figure **1.21(b)** was measured after the same cathode was cleaned with the UV drive laser and low power RF and then continuous operated at high RF power for approximately 1½ years. The area illuminated by the 2 mm diameter laser beam is easily seen in the emission image. Its size gives the magnification of the electron optics between the cathode and the view screen. The dark, irregular regions approximately a few

100 µm in size are likely due to the different work functions of the grains of the poly crystalline composition of the copper cathode. The bright, red-yellow regions appear clustered around the edge of these dark grains and are likely due to enhanced photoemission by adsorbed molecules from the vacuum.

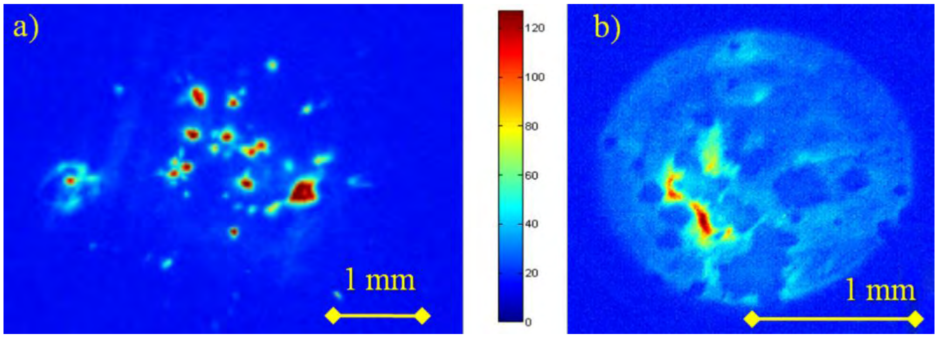

Figure 1.21. Examples of electron beam images on a view screen with the solenoid adjusted to obtain an image of the electron image from the cathode when illuminated by a large laser spot. The bunch charge is 9 pC. The observed magnification was -3.6, the integrated field strength was 0.5165 kG m, L_2 = 1.066 m and the solenoid effective length is 0.1935 m. These parameters give a solenoid wave number of 6.75 per meter with the beam rotating 74.8° in the solenoid. The solenoid focal length is 15.3 cm.

1.5.2 Chromatic Aberration of the Solenoid

The beam's energy spread can introduce additional emittance in the solenoid due to different electrons having different focal lengths. This emittance can be computed by starting with the symmetric transverse beam matrix, σ_{beam}, and the transformation for a thin lens. The beam matrix is defined as

$$\sigma \equiv \begin{pmatrix} \sigma_{11} & \sigma_{12} \\ \sigma_{12} & \sigma_{22} \end{pmatrix} \tag{1.77}$$

The transformation of the beam matrix though the thin lens is given by

$$\sigma(1) = R_{lens}\sigma(0)R_{lens}^T = \begin{pmatrix} 1 & 0 \\ -1/f & 1 \end{pmatrix}\begin{pmatrix} \sigma_{11} & \sigma_{12} \\ \sigma_{12} & \sigma_{22} \end{pmatrix}\begin{pmatrix} 1 & -1/f \\ 0 & 1 \end{pmatrix} \tag{1.78}$$

Performing the matrix multiplications gives

$$\sigma(1) = \begin{pmatrix} \sigma_{11} & \sigma_{12} - \dfrac{\sigma_{11}}{f} \\ \sigma_{12} - \dfrac{\sigma_{11}}{f} & \sigma_{22} + \dfrac{\sigma_{11}}{f^2} - \dfrac{2\sigma_{12}}{f} \end{pmatrix} \tag{1.79}$$

The change due to a variation in the beam momentum, Δp, can be obtained from the derivative of the beam matrix, $\Delta\sigma_{beam}$**(**1**)**, as

$$\Delta\sigma_{beam}(1) = \frac{d\sigma}{dp}\Delta p = \begin{pmatrix} 0 & -\sigma_{11}\dfrac{d}{dp}\left(\dfrac{1}{f}\right) \\ -\sigma_{11}\dfrac{d}{dp}\left(\dfrac{1}{f}\right) & \cdots \end{pmatrix}\Delta p \tag{1.80}$$

There is no need to compute the $\sigma_{22}(\mathbf{1})$ matrix element because it gets multiplied by zero when the emittance is computed

$$\varepsilon_{n,chromatic} = \beta\gamma\sqrt{\det(\Delta\sigma_{beam}(\mathbf{1}))} = \beta\gamma\sigma_x^2\left|\frac{\mathrm{d}}{\mathrm{d}p}\left(\frac{1}{f}\right)\right|\sigma_p \tag{1.81}$$

where $\sigma_{11} = \sigma_x^2$ has been used and β is the beam velocity divided by the speed of light, γ is the beam's Lorentz factor, $\sigma_{x,sol}$ is the transverse rms beam size at the entrance to the solenoid, and σ_p is the rms momentum spread of the beam. This is a general expression for the chromatic emittance of a thin lens. For a solenoid lens in the rotating frame of the beam, the focal strength is given by

$$\frac{1}{f_{sol}} = K\sin(KL_{sol}) \tag{1.82}$$

Using this and other quantities for the solenoid in Equ. 1.81 results in the following expression for the normalized chromatic emittance of a solenoid

$$\varepsilon_{n,chromatic} = \beta\gamma\sigma_{x,sol}^2\, K\,|\sin(KL) + KL\cos(KL)|\,\frac{\sigma_p}{p} \tag{1.83}$$

Figure **1.22** is a plot the chromatic emittance as a function of the energy spread as given by Equ. 1.83 and by simulation [1.35]. There is excellent agreement between the analytic and numerical approaches. The simulation used an initial beam with zero emittance with zero divergence entering the solenoid. The plot assumes an rms beam size of 1 mm. The typical measured full bunch (projected) and time-sliced (slice) electron energy spreads are indicated showing the chromatic emittance to be ~0.3 μm for the projected emittance and 0.02-0.03 μm for the slice chromatic emittance. This should be compared with the measured LCLS projected emittance of 0.4-0.5 μm for 250 pC.

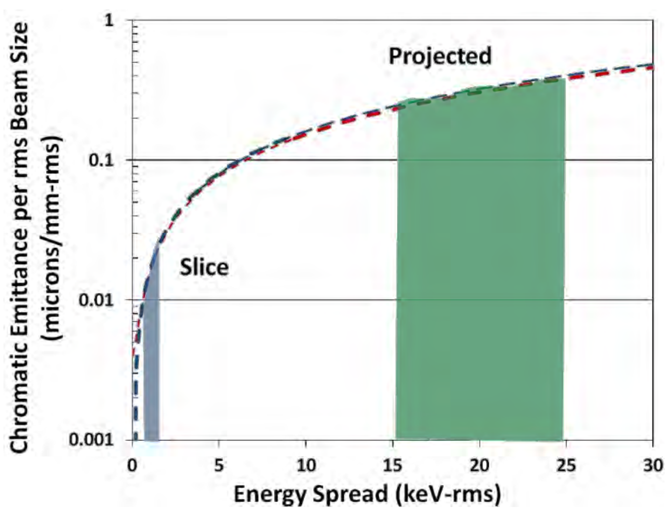

Figure 1.22. Comparison of the chromatic emittance given by Equ. 1.83 (dashed red) and the emittance computed using the GPT particle pusher code (dashed blue) vs. rms energy spread. Both calculations assume the beam size at the solenoid is 1 mm-rms. The typical measured full bunch (projected) and time-slice (slice) electron energy spreads are indicated by the blue and green regions.

While the solenoid's chromatic aberration can be a significant part of the projected emittance, its contribution is much less for the slice emittance. This is because the rms slice energy spread is small and thought to be 1 keV or less at 250 pC. Thus, the chromatic emittance for a slice is only ~0.02 μm (mm rms)$^{-1}$. It is important to note that because the beam size at the solenoid lens enters to the second power in Equ. 1.83, the chromaticity can introduce considerable emittance if the beam is large. Therefore, the beam size at the solenoid should be reduced in future gun designs.

1.5.3 Geometric Aberrations

It is known that all magnetic solenoids exhibit a 3rd-order aberration, also known as the spherical aberration. This aberration is mostly located at the ends of the solenoid since it depends upon the second derivative of the axial field with respect to the beam direction [1.36]. In theory, the spherical aberration could be computed from the solenoid's magnetic field; in practice, this is difficult and doesn't take into account all the important details of the beam dynamics. Therefore, in order to numerically isolate the geometrical aberration from other effects, a simulation was performed with only the solenoid followed by a simple drift. Maxwell's equations were used to extrapolate the measured axial magnetic field, $B_z(z)$, and obtain the radial fields [1.35]. Following traditional optical analysis, an initial beam distribution of a square, 2 mm × 2 mm, was used assuming perfect collimation (zero divergence = zero emittance), zero energy spread and an energy of 6 MeV. The simulated transverse beam profiles given in Figure **1.23** show how an otherwise "perfect" solenoid has the characteristic "pincushion" distortion [1.37]. A 4 mm × 4 mm (edge-to-edge) object gives 0.01 μm emittance, while 2 mm × 2 mm square results in only 0.0025 μm.

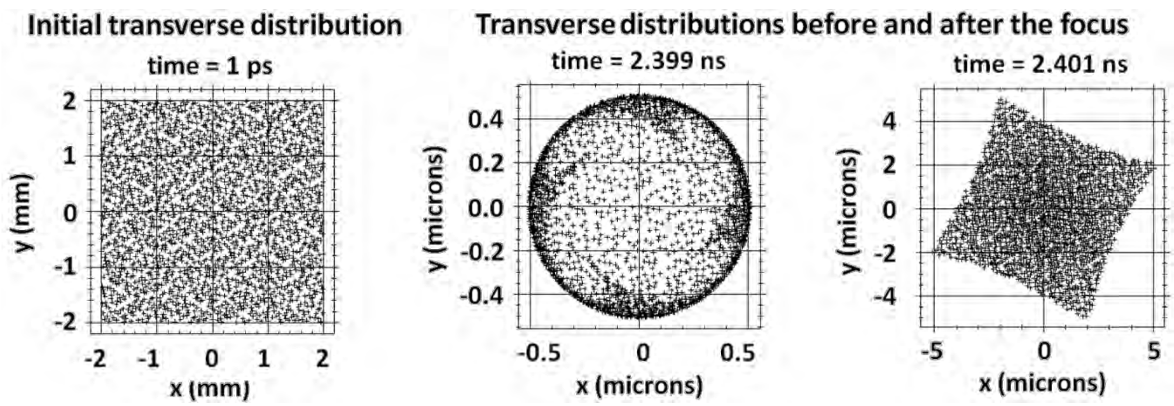

Figure 1.23. Ray-tracing simulation of the transverse beam distribution due to the geometric aberration of a solenoid. Left: The initial transverse particle distribution before the solenoid with zero emittance and energy spread. Center: The transverse beam distribution occurring slightly before the beam focus after the solenoid illustrating the third-order distortion. Right: The beam distribution immediately after the beam focus showing the characteristic "pincushion" shape of the rotated geometric aberration.

Figure **1.24** shows the simulation for a uniformly round beam with initially zero emittance as a function of rms beam size at the entrance of the solenoid. In addition to the simulation, the green curve gives a 4th-order polynomial fit to the simulated emittance. It is still necessary to understand why the simulation indicates a 4th-order dependence with beam size, rather than the expected 3rd-order, spherical.

1.5.4 Aberrations due to Anomalous Quadrupole Fields and Emittance Recovery

Beam studies can show an astigmatic (unequal *x*- and *y*-plane focusing) beam from an RF gun due either to the single-side RF feed or to the magnetic field asymmetries of the gun solenoid. In order to understand and distinguish between these effects, the solenoid's multipole magnetic field was measured using a rotating coil. The magnetic measurements showed small quadrupole fields at the ends of the solenoid with equivalent focal lengths at 6 MeV of 20-30 m for the GTF solenoid. However, even though these fields were weak, it was decided to install normal and skew quadrupole correctors inside the bore of the solenoid to correct them. The details of how the correctors were incorporated into the gun are given in [1.38] and their use during operation is described in [1.39].

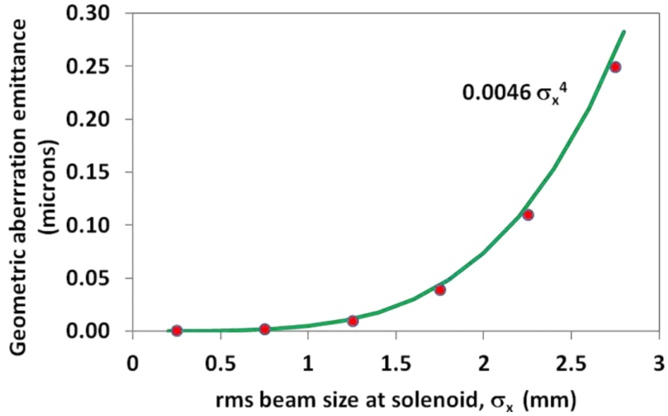

Figure 1.24. The geometric aberration for the gun solenoid: emittance vs. the *x*-rms beam size at the lens. The emittance computed with GPT (points red) compared with a fourth order fit (solid green). The simulation used the axial magnetic field obtained from magnetic field measurements of a solenoid (Figure 1.25). The initial beam had zero emittance.

Figure **1.25** shows the axial magnetic field and the quadrupole magnetic field and its rotation or phase angle along the beam axis of the LCLS solenoid. The quadrupole field was measured using a rotating coil with a 2.8 cm radius, which is the radius for which the quadrupole field is given. The quadrupole phase angle is the angular rotation of the poles relative to an aligned quadrupole. The phase angle is the angle of the north pole relative to the *y*-axis (left when travelling in the beam direction) for a beam-centric, right-handed coordinate system. In this coordinate system a normal quadrupole has a phase angle of 45˚. The difference in phase angle between the entrance (z = -9.6 cm) quadrupole field and the exit (z = +9.6 cm) field angle is close to 90˚ and both fields change sign when the solenoid's polarity is reversed. These are similar effects as measured previously for the GTF solenoid, although, the LCLS solenoid had weaker quadrupole fields with equivalent focal lengths of 50-70 m, instead of 20-30 m, as noted above for GTF.

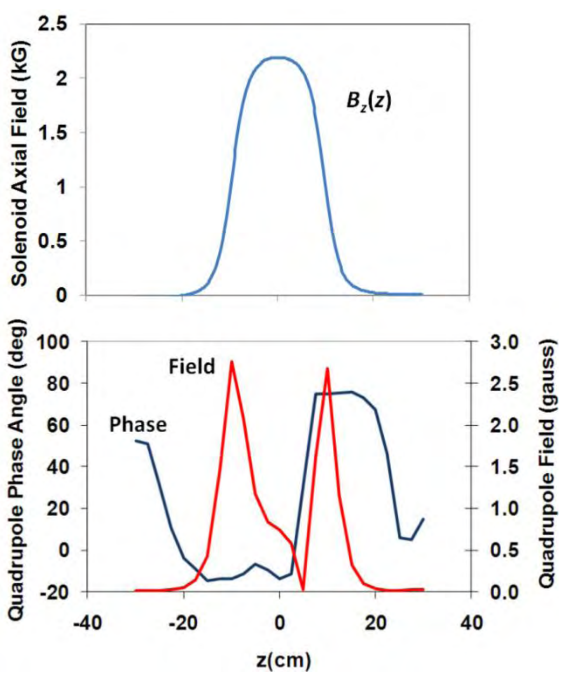

Figure 1.25. Magnetic measurements of the LCLS gun solenoid. Top: Hall probe measurements of the solenoid axial field. The transverse location of the measurement axis (the *z*-axis) was determined by minimizing the dipole field. Bottom: Rotating coil measurements of the quadrupole field. The rotating coil dimensions were 2.5 cm long with a 2.8 cm radius. The measured quadrupole field is thus the average over these dimensions.

As described earlier, the correction of these field errors was done by installing normal and skew quadrupoles inside the bore of the solenoid. The effect these correction quadrupoles have upon the emittance is quite profound, as can be seen in Figure **1.26** where the emittance for 1 nC and 250 pC are plotted vs. the normal corrector quadrupole strength.

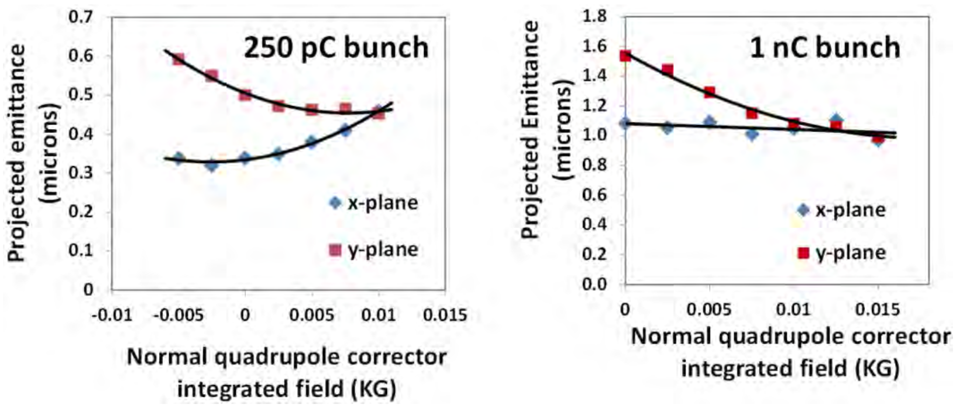

Figure 1.26. a) Measured *x*-plane (blue) and *y*-plane (red) emittances vs. the normal corrector quadrupole strength for a 1 nC bunch charge. b) Behavior observed for 250 pC.

The beam emittance due to these anomalous quadrupole fields can be computed both in simulation and analytically. The analysis begins by assuming a simple thin quadrupole lens followed by a solenoid with the 4×4 *x*-*y* beam coordinate transformation [1.34] given by

$$R_{sol}R_{quad}=\begin{pmatrix} \cos^2 KL & \dfrac{\sin KL\cos KL}{K} & \sin KL\cos KL & \dfrac{\sin^2 KL}{K} \\ -K\sin KL\cos KL & \cos^2 KL & -K\sin^2 KL & \sin KL\cos KL \\ -\sin KL\cos KL & -\dfrac{\sin^2 KL}{K} & \cos^2 KL & \dfrac{\sin KL\cos KL}{K} \\ K\sin^2 KL & -\sin KL\cos KL & -K\sin KL\cos KL & \cos^2 KL \end{pmatrix}\begin{pmatrix} 1 & 0 & 0 & 0 \\ -\dfrac{1}{f_q} & 1 & 0 & 0 \\ 0 & 0 & 1 & 0 \\ 0 & 0 & \dfrac{1}{f_q} & 1 \end{pmatrix} \quad (1.84)$$

As in the derivation of the chromatic emittance: L is the effective length of the solenoid and

$$K=\frac{B_z(0)}{2(B\rho)_0} \quad (1.85)$$

where $B_z(0)$ is the interior axial magnetic field of the solenoid, $(B\rho)_0$ is the magnetic beam rigidity, and f_q is the focal length of the anomalous quadrupole field. The beam rotates through the angle KL in the solenoid.

The 4×4 beam matrix after the combined quadrupole and solenoid, is then

$$\sigma_{beam}(1)=(R_{sol}R_{quad})\,\sigma_{beam}(0)\,(R_{sol}R_{quad})^{T} \quad (1.86)$$

and the *x*-plane emittance after the quadrupole and solenoid is given by the determinate of the 2×2 sub-matrix,

$$\varepsilon_{x,qs} = \beta\gamma\sqrt{\det\sigma_x(1)} = \beta\gamma\sqrt{\det\begin{pmatrix}\sigma_{11}(1) & \sigma_{12}(1)\\ \sigma_{12}(1) & \sigma_{22}(1)\end{pmatrix}} \tag{1.87}$$

Finally, the normalize emittance is found to be

$$\varepsilon_{x,qs} = \beta\gamma\sigma_{x,sol}\sigma_{y,sol}\left|\frac{\sin(2KL)}{f_q}\right| \tag{1.88}$$

The *x*- and *y*-transverse rms beam sizes are the entrance to the solenoid are $\sigma_{x,sol}$ and $\sigma_{y,sol}$.

Figure **1.27** compares this simple formula (Equ. 1.88) with a particle tracking code [1.35] for the case of an initial beam with zero emittance, zero energy spread and assuming a round beam. The normalized emittance is plotted. For the comparison, assume the quadrupole focal length is 50 m, which is approximately the same as given by the magnetic measurements for the LCLS solenoid at 6 MeV. Both the analytic theory and the simulation assume a quadrupole field only at the solenoid's entrance. And of course, the simulation includes both this quadrupole effect and the geometric aberration described above. The good agreement verifies the model's basic assumptions and illustrates how a very weak quadrupole field can strongly affect the emittance when combined with the rotation in a solenoid field.

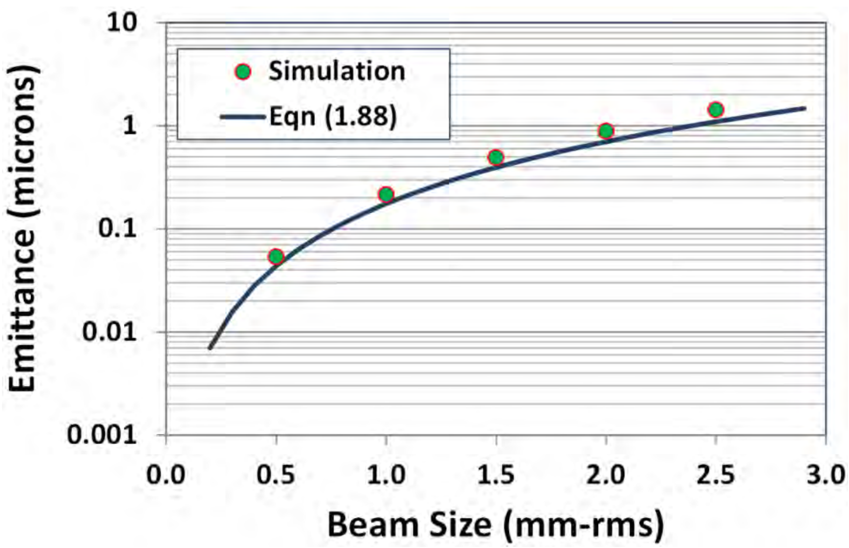

Figure 1.27. Comparison of the emittance due to the quadrupole-solenoid coupling given by Equ. 1.88 with a particle tracking simulation for the case of the LCLS solenoid. For a beam energy of 6 MeV the quadrupole focal length was 50 m and the solenoid had an integrated field of 0.46 KG-m.

The above expression is for the case of a quadrupole plus solenoid system where the quadrupole itself isn't rotated. When the quadrupole is rotated about the beam axis by angle α with respect to the normal quadrupole orientation, then total rotation angle becomes the sum of the quadrupole rotation plus the beam rotation in the solenoid. Then, the emittance becomes

$$\varepsilon_{x,qs} = \beta\gamma\sigma_{x,sol}\sigma_{y,sol}\left|\frac{\sin(2(KL+\alpha))}{f_q}\right| \tag{1.89}$$

Figure **1.28** compares Equ. 1.89 with a simulation for a 50 m focal length quadrupole followed by a strong solenoid (focal length of ~15 cm). Both show the emittance becoming zero whenever $KL + \alpha = n\pi$. The first

zero of the emittance occurring at negative quadrupole angle (not shown) is the beam rotation in the solenoid. The slight shift in angle between the theory and simulation results because the solenoid in the simulation has fringe fields which are ignored in the theory.
The final emittance is due to three effects: The skew angle and focal length of the entrance quadrupole (α_1,f_1), the rotation in the solenoid (KL) and the skew angle and focal length of the exit quadrupole (α_2,f_2). Combining the entrance quadrupole skew angle with the solenoid rotation, one obtains the emittance for a solenoid with quadrupole end fields,

$$\varepsilon_{x,total} = \beta\gamma\sigma_{x,sol}\sigma_{y,sol}\left|\frac{\sin(2(KL+\alpha_1))}{f_1}+\frac{\sin(2\alpha_2)}{f_2}\right| \tag{1.90}$$

It is relevant to point out some of the features of Equ. 1.90. First, consider the situation when both quadrupoles are perfectly aligned without any skew, *i.e.*, $\alpha_1 = \alpha_2 = 0$, then while there's no emittance contribution from the exit quadrupole, the entrance quadrupole still appears skewed by the beam's rotation in the solenoid and the emittance increases unless there is no entrance quadrupole field. For this case, the emittance does not depend upon the polarity of the solenoid field. However, this is not true for α_1, $\alpha_2 \neq 0$. Equ. 1.90 also shows the emittance changes if the polarity of the solenoid field is reversed when there is a skewed quadrupole field: further details of this effect are discussed in the next section. Finally, the formula indicates that adding independently powered skew and normal quadrupoles after the solenoid can cancel this effect and recover the initial emittance or long wire skew and normal quadrupole correctors installed inside the solenoid can also be used for this cancellation, as was done in the LCLS solenoid [1.38].

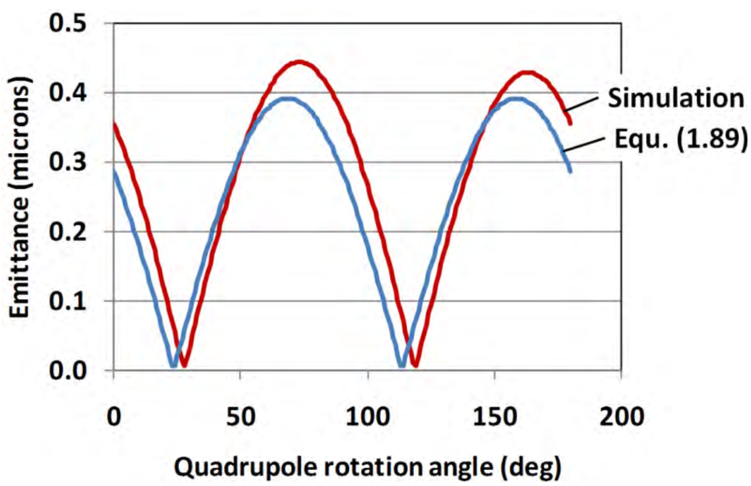

Figure 1.28. The emittance for a quadrupole-solenoid system plotted as a function of the quadrupole rotation angle. The theory emittance (solid blue) is computed using Equ. 1.89 and the simulation (solid red) is done with the GPT code. The beam size at the solenoid is 1 mm rms for both the *x*- and *y*-planes.

The emittance growth due to the solenoid's anomalous quadrupole fields can be compensated with the addition of skew and normal corrector quadrupoles, as shown by Equ. 1.90. Two quadrupoles, one normal and one skewed, are needed to produce the proper field strength and rotation angle. In the LCLS solenoid, these correctors consist of eight long wires inside the solenoid field, four in a normal quadrupole configuration and four arranged with a skewed quadrupole angle of 45˚. Thus, since corrector quadrupoles overlap the solenoid field, one would expect their skew angles should be added to KL, similar to the first term of Equ. 1.90. The emittance due to the composite system of a rotated quadrupole in front of the solenoid, the two corrector quadrupoles inside the solenoid, and the exit rotated quadrupole can be computed as the following sum

$$\varepsilon_{x,total} = \beta\gamma\sigma_{x,sol}\sigma_{y,sol}\left|\frac{\sin(2(KL+\alpha_1))}{f_1}+\frac{\sin(2KL)}{f_{normal}}+\frac{\sin(2(KL+\pi/4))}{f_{skew}}+\frac{\sin(2\alpha_2)}{f_2}\right| \quad (1.91)$$

The first and fourth terms inside the absolute value brackets are due to the entrance and exit quadrupoles with focal lengths f_1 and f_2 and skew angles of α_1 and α_2, respectively. The second and third terms are approximations for the normal and skew corrector quadrupoles with focal lengths f_{normal} and f_{skew}, respectively, and of course the skew angles of the normal and skew corrector quadrupoles are 0 and $\pi/4$.

Figure **1.29** illustrates the emittance due to these effects as a function of the normal and skew corrector quadrupole focal lengths using Equ. 1.91. The entrance and exit anomalous quadrupole focal lengths are 50 m and their rotation angles as indicated by Figure **1.29** are -60˚ and 25˚, respectively. The red curves are for the normal corrector quadrupole only with the skew corrector quadrupole off, while the blue curves are given for the skew quadrupole only with the normal quadrupole off. The zero of emittance is shifted for the two correctors since the overall rotation necessary to correct the error fields is neither normal nor skewed, but something in between. Both solid curves asymptotically converge to the uncorrected emittance as the correctors are turned off (infinite focal length). The figure also shows the effect of reversing the polarity of the solenoid with corresponding emittances plot as dashed lines. In this case, the uncorrected emittance clearly approaches a much smaller emittance. As mentioned earlier, the skewed anomalous quadrupole fields make the resulting emittance growth and focusing of the solenoid dependent upon its polarity and provide an experimental signature that the fields are skewed. Therefore, if the anomalous fields are skewed, even with no quadrupole correction, one polarity of the solenoid results in a lower emittance than the other.

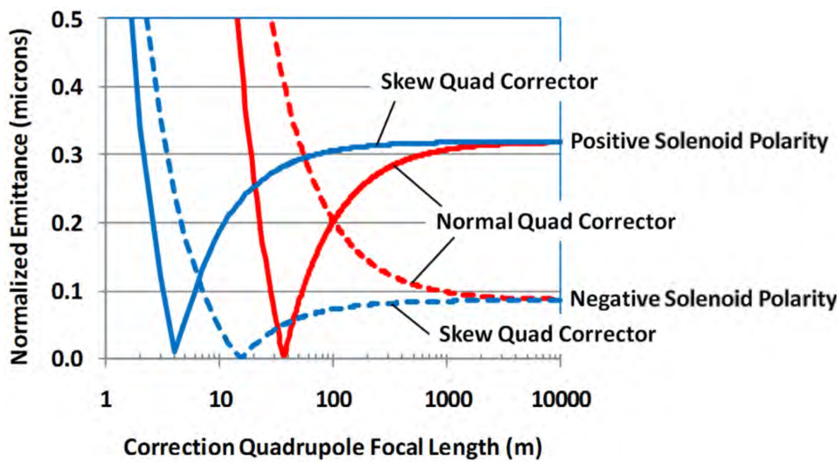

Figure 1.29. The emittance as a function of the normal and skew quadrupole corrector focal lengths for positive and negative polarities of the solenoid. Anomalous quadrupole field errors with 50 m focal lengths are included at the ends of the solenoid with rotations of -60˚ and 25˚, respectively, as given in Figure 1.25. The *x*- and *y*-rms beam sizes at the solenoid entrance are assumed to be 1 mm.

1.6 SPACE CHARGE SHAPING

The space charge force can defocus the beam, behaving similar to a negative focal length lens. While most emittance compensation techniques use external fields to cancel the linear space charge effects, it is the non-linear space charge forces which produce additional emittance. In this section, the radial and longitudinal electric fields inside a rotationally symmetric bunch are given in terms of a power series expansion about the bunch longitudinal axial. This derivation is for the steady-state case, without currents or time dependent fields. It gives the fields in the rest frame of the bunch, which for the example considered here, is thin and disk-like.

Here, we derive the radial force on an electron confined to a thin disk of charge. The surface charge density is assumed to be rotational symmetric with a radial quadratic dependence upon the surface charge density. The result is that the quadratic radial distribution can be adjusted to cancel the 3rd-order space charge defocus of the disk's distribution, Figure **1.30**. The technique is to first compute the electrical potential energy along the axis of rotation of the disk. Expanding this potential into a power series, we multiply each term by the appropriate order of Legendre polynomial to obtain the potential at any point on space. Finally, the divergence of the potential gives the radial electric field on an electron.

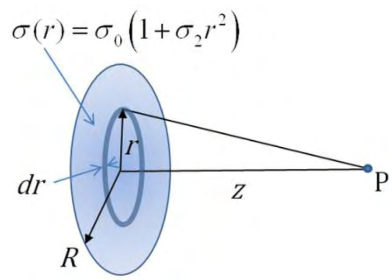

Figure 1.30. The geometry for computing the on-axis electric field produced by a disk of charge.

The electric potential along the disk's axis can be computed using the following integral

$$4\pi\varepsilon_0 V(z) = \iint \frac{\sigma}{\sqrt{z^2+r^2}}ds = 2\pi\int_0^R \frac{\sigma(r)r}{\sqrt{z^2+r^2}}dr \tag{1.92}$$

where surface charge density as a function of r is $\sigma(r) = \sigma_0(1 + \sigma_2 r^2)$, then the integrand has two parts. One linear and the other third-order in r, as given by

$$V(z) = \frac{\sigma_0}{2\varepsilon_0}\left(\int_0^R \frac{r}{\sqrt{z^2+r^2}}dr + \sigma_2\int_0^R \frac{r^3}{\sqrt{z^2+r^2}}dr\right) \tag{1.93}$$

Performing the integration gives

$$V(z) = \frac{\sigma_0}{2\varepsilon_0}\left\{\sqrt{z^2+R^2} - z + \sigma_2\left[\frac{1}{3}(z^2+R^2)^{3/2} - z^2\sqrt{z^2+R^2} + \frac{2}{3}z^3\right]\right\} \tag{1.94}$$

The first two terms inside the outer brackets give the on-axis potential for a uniform disk. The σ_2 term is the potential coming from the parabolic radial part of the surface charge density. For a beam that is off-axis, we implement the following coordinate as seen in Figure **1.31**.

Consider the uniform part of the charge distribution first. Expanding the potential as a power series, grouping into terms with the same power and then multiplying each term with the Legendre polynomial of that power, gives the potential everywhere. The electric potential to 4th-order is then

$$V_0(\theta,r) = \frac{\sigma_0}{2\varepsilon_0}\left[R - rP_1(\cos(\theta)) + \frac{1}{2}\frac{r^2}{R}P_2(\cos(\theta)) - \frac{1}{8}\frac{r^4}{R^3}P_4(\cos(\theta)) + \ldots\right] \tag{1.95}$$

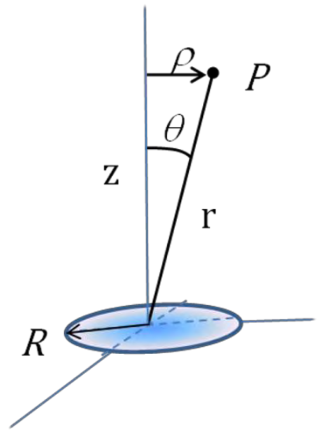

Figure 1.31. Coordinates used to compute the off-axis electric field of a charged disk.

Following the same procedure for the parabolic part of the charge density gives the electric potential due to the quadratic σ_2 in the plane for the disk as

$$V_2(\rho) = \frac{\sigma_0\sigma_2}{2\varepsilon_0}\left[\frac{1}{3}R + \frac{1}{4}R\rho^2 - \left(\frac{3}{8}\right)^2\frac{\rho^4}{R} + \ldots\right] \tag{1.97}$$

where the total potential is the sum, $V(\rho) = V_0(\rho) + V_2(\rho)$. The radial electric field is given by $E_\rho(\rho) = \frac{\partial V}{\partial \rho}$, or to third-order

$$E_\rho(\rho) = \frac{\sigma_0}{2\varepsilon_0}\left[\left(\frac{\sigma_2}{2}R - \frac{1}{2R}\right)\rho - \frac{3}{16}\left(3\sigma_2 + \frac{1}{R^2}\right)\frac{\rho^3}{R}\right] \tag{1.98}$$

Notice, that if $\sigma_2 = \frac{-1}{3R^2}$, then the third order term is zero when the radial charge density is parabolic

$$\sigma(\rho) = \sigma_0\left(1 - \frac{\rho^2}{3R^2}\right) \tag{1.99}$$

In this case and the radial space charge force becomes linear

$$E_\rho(\rho) = \frac{-\sigma_0}{3\varepsilon_0}\frac{\rho}{R} \tag{1.100}$$

and the beam expands linearly with little increase in the emittance. The parabolic radial distribution is plotted in Figure **1.32**.

The above description follows the seminal work of Serafini [1.40] who first proposed shaping in RF guns to reduce the non-linear space charge emittance. More recently, Luiten [1.41] has applied classical stellar dynamics to the problem and performed simulations showing that a hemispherical-shaped surface charge density at the cathode rapidly expands into a uniform 3-D ellipsoid distribution having linear space charge forces and no space charge emittance. Therefore, the precise radial shaping of the electron bunch using the drive laser should reduce the non-linear space charge emittance.

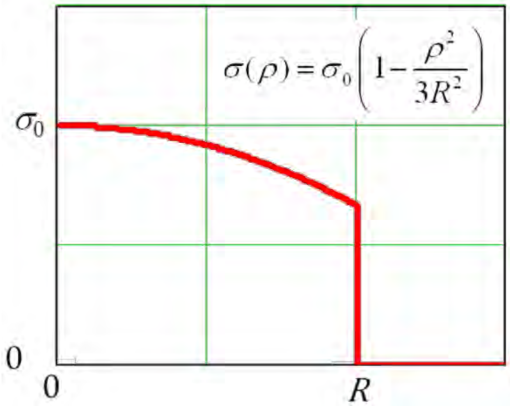

Figure 1.32. Plot of the radial charge distribution having no 3rd-order space charge force.

1.7 SIMULATION CODES

Simulation codes are critical components of the photoinjector design process and are an area of continual development. This section describes some of the more common codes used for photoinjector development, with an emphasis on codes that can be used effectively on a typical desktop computer.

1.7.1 General Comments on Simulation Fidelity

In the most general terms, operation of a photoinjector can be described by the following process:

1) A laser beam strikes the cathode.
2) Electrons are emitted from the cathode.
3) The emitted electrons interact, *via* electromagnetic fields, with
   a) the photoinjector,
   b) other components such as solenoids,
   c) each other, and
   d) the electron emission process.

Ideally, the process results in the production of a high quality electron beam. The simulation codes used in injector design to handle each of these steps with varying fidelity to the real world.

The typical goal of a beam dynamics simulation code is, broadly speaking, to provide the 6-D coordinates of particles within the beam at the end of the simulation. Every beam property of interest – emittance, energy spread, bunch duration, *etc.* – can be calculated from this distribution.

Most photoinjector simulations that work with distributions of particles are based upon stepping forward in time. At each time step, the motion of all particles and the forces acting upon them are calculated and updated. Depending on the simulation code used, time steps may be fixed or variable; typical time steps are on the order of 0.1-10 ps, with finer steps taken when the beam is being emitted from the cathode and larger steps when the beam is in regions of slowly varying external fields.
A "typical" bunch charge might be -1 nC, comprised of approximately 6.4×10^9 electrons. ~0.15 TB would be required to store every electron's position in 6-D phase space with quadruple-precision (32-bit) floating point numbers. Modern desktop computers do not typically have that much memory and only recently have cluster computers progressed to the point where each electron in a bunch could be independently tracked. Further, the time to execute the simulation generally scales at least as fast as the number of particles within

the simulation. Thus, often the first reduction in fidelity that occurs is to use a "macroparticle" to represent a larger number of electrons in the bunch. In a desktop simulation, typically done as part of an initial design study, perhaps 10^4-10^5 macroparticles might be used to provide a tractable number of particles from both computer memory and CPU time perspectives.

In most photoinjector simulations, all macroparticles are assigned the same charge, but with different charge density within the electron beam (say, from a non-uniform drive laser) reflected by different spatial density of macroparticles. This simplifies the macroparticle bookkeeping and various other computational tasks, but can yield "noisy" results and errors when the number density in the simulated beam is too low. An alternate approach is to keep the initial number density of macroparticles constant, but varying the charge per macroparticle to reflect density variations within the electron beam. The former approach is generally the one used in injector simulations, and the typical method of reducing noise is to increase the number of macroparticles or, *via* "quiet start," non-random distributions. The latter may be more suitable to the introduction of cathode physics into the beam dynamics codes.

Electron emission, encompassed by cathode theory and modeling, is a rich area of current development and is treated more fully in Chapter 5. Historically, most beam dynamics codes have not incorporated physics-based emission modeling, and so will not be discussed in great detail here. Rather, most beam dynamics codes allow the user to specify, for instance, the emission of macroparticles vs. time over a given area of the cathode; this may be done *via* supplying an external distribution or by specifying various parameters of the distribution.

Another commonly used approximation is the assumption of radial symmetry of RF and magnetic fields within the accelerating structures and beamlines, and of the beam's self-fields. For initial studies and for some photoinjector designs (such as RF photoinjectors with on-axis power couplers), this is not a bad approximation; however, it does represent an additional loss of fidelity with respect to the physical reality of the system being modeled, and of necessity excludes the impact of both TE modes and magnetic field aberrations such as those described in Section 1.5, as well as asymmetries arising in the accelerating fields from the presence of RF power couplers, field probes, viewports, *etc.* Radial symmetry of the beam's self-fields is clearly broken as soon as the beam passes through a quadrupole, or indeed any multipole beamline element.

The interaction of the beam with itself, a.k.a. "space charge effects," is central to the emittance compensation process. While in principle space charge forces can be calculated from every particle to every other particle, the time required to perform such a calculation scales as N^2, where N is the number of macroparticles in the simulation. Most beam dynamics codes therefore use a variation of a particle-in-cell, or PIC, method to calculate space charge effects. The codes are grouped into one of two general categories. If the code ignores the interaction of the beam with the photoinjector structure, it is known as a particle-pusher (or sometimes pseudo-PIC) code. If such interactions are accounted for in a self-consistent fashion, the code is referred to as a particle-in-cell, or PIC, code.

Finally, electromagnetic (EM) design codes are used to simulate the physical structures, such as RF cavities, DC gaps, solenoids, *etc.*, used in the photoinjector design process. As with beam dynamics codes, EM design codes differ widely in their capabilities, fidelity and ease of use. An important consideration is how readily information (primarily as field maps) can be transferred from EM design codes to beam dynamics codes.

Table **1.1** is a partial listing of simulation codes useful for photoinjector design. It is by no means a complete list and reflects the authors' experiences and predilections.

Name	**Type**	**Notes**
POISSON / SUPERFISH	2-D electro-, Magnetostatic and RF Code	Integrates well with PARMELA and GPT; TM RF Modes Only; Extensive Documentation.
CST Microwave Studio	2-D and 3-D EM Modeling Code	General-purpose Very Powerful electromagnetic Modeling Code; Excellent Documentation; Some Beam Transport; Commercial Code
MAFIA	2-D and 3-D EM Modeling Code	General-purpose Very Powerful Electromagnetic Modeling Code; Excellent Documentation; Some Beam Transport; Commercial Code
TRANSPORT	Envelope Code	The "Grandfather" Code; Manual is an Excellent Reference for 1st-order Transport Matrices of Accelerator Components.
TRACE-3D	Envelope Code with Space Charge	Fast; Good Graphical Tools Available
HOMDYN	Envelope Code	
PARMELA	Particle Pusher	Includes many "Built-in" Accelerator Elements; Well-benchmarked; Good Documentation; Source Code not Available
T-Step	Particle Pusher	Upgraded Version of PARMELA; Commercial Code
ASTRA	Particle Pusher	Many Variations; Often the Code of Choice for Implementing Genetic Algorithm-based Optimization
GPT	Particle Pusher	Includes many "Built-in" Elements; New Elements can be Added by the User; Extensive Options for Importing Field Maps; Unusual, but Useful Coordinate Scheme; Commercial Code
IMPACT-T	Particle Pusher	Under Wide Development; Several Variants
SPIFFE	2-D PIC Code	Basic Code; Fast; Good Learning Tool
VORPAL	3-D PIC Code	Includes Updated Cathode Modeling; Commercial Code
MICHELLE	3-D PIC Code	Focuses on Electron Gun Design; Commercial Code
MAD	High-energy	
ELEGANT	High-energy	Includes CSR and Longitudinal Space Charge Models; Used in LCLS Design

Table 1.1. List of simulation codes with some description.

1.7.2 Particle Pushers

Particle pusher codes are beam dynamics codes which do not consider the interaction of the electron beam with the structure of the photoinjector. Injector beam dynamics codes must include space charge effects however, and this is often done *via* a PIC-like methodology.

In a typical pseudo-PIC calculation, a grid (2-D or 3-D) is overlaid upon the particle distribution. Each macroparticle's charge is assigned either to its nearest grid point, or split over the grid points of its encompassing cell according to its position within the cell. Maxwell's equations are then solved on the grid; the resulting fields are applied to the macroparticles and the next simulation time step is taken. Computation time scales approximately as $M * N$, where M is the number of grid points and N is, again, the number of macroparticles. A 2-D PIC implementation in essence treats every particle as a ring of charge; this approximation breaks down, to a greater or lesser degree, as soon as radially asymmetric charge distributions (from the cathode, passing through a quadrupole field, *etc.*) are encountered. In either a 2-D or a 3-D PIC code, there must be enough cells to sufficiently model local charge density variation of interest, but not so many that the statistics of assigning charge to the grid become poor. As importantly, there must be sufficient numbers of macroparticles to maintain good statistics for the space charge calculation.

Typical particle pusher codes, including PARMELA [1.42], T-Step [1.43], IMPACT-T [1.44], [1.45], GPT [1.35] and Astra [1.46] usually offer one or several PIC-like algorithm to calculate space charge effects. (PARMELA, for instance, can perform either a 2-D or a 3-D space charge calculation.) The “external” fields, such as those from DC gaps, RF cavities, solenoids and the like, are just that – typically provided by a field map generated by an external code, the fields from these elements are applied to the macroparticles, but the macroparticles cannot modify those fields. An example of such a calculated external field can be seen in the top of Figure **1.6**. The simulation neither knows nor cares where the physical boundaries of the photoinjector are, save perhaps specified radii beyond which macroparticles are assumed to have struck a wall and consequently be removed from the simulation. Likewise, there is no guarantee that the applied fields are consistent with the cavity geometry.

This pseudo-PIC approach has several advantages. Since the PIC mesh need to extend only over the electron beam, a high density of mesh cells can be used for modest memory expense; and if the mesh expands and contracts with the beam, the approximate macroparticle density within the mesh can be held steady, helping to preserve the statistics of the calculation.

To further save time, some pseudo-PIC codes perform a relativistic transformation to the average rest frame of the beam before applying the grid. The general assumption made is that in this frame the particles have negligible velocity, so only Poisson’s equation need be solved and the fields are then transformed back to the laboratory frame. The main disadvantage of this approach is that it breaks down when beams have large velocity spreads, or large fractional spreads ($\Delta\gamma/\gamma$).

A general disadvantage of the particle pusher codes is they cannot self-consistently calculate the interaction of the beam with the structure of the injector. This can become very important when, for instance, attempting to simulate beam loading or wakefield effects. Also, as the electromagnetic fields are generally not self-consistent, incorporation of advanced electron emission models into these codes, particularly in the case of multi-bunch emission, can be problematic.

1.7.3 Particle-in-Cell Codes

Rather than applying a mesh over only the macroparticles, a true PIC code applies the mesh to the entire geometry, within which the beam can propagate, incorporating all boundary surfaces the beam can “see.” The mesh is generally fixed in space rather than moving with the beam.

Depending on the PIC code, the fields used to accelerate and guide the beam can either be imported as with the particle pusher codes, calculated by the PIC code itself, or by some combination of the two methods.

PIC codes have several significant advantages. They are generally fully electromagnetically self-consistent, so beams with large energy or velocity spreads are handled properly. Boundary conditions are automatically incorporated as the injector geometry, so the PIC grids are properly terminated at their edges and impedance effects can be included, as well as particle beam wakefields. This also allows incorporation of cathode emission models that require accurate values for the electromagnetic fields at the cathode surface to calculate emission current density … whether or not the beam is within the vicinity of the cathode.

Finally, advanced 3-D PIC codes, such as VORPAL [1.47], can be used to perform most of the calculations required to model an injector, including RF power couplers, the buildup of accelerating fields, multipacting and the extraction of beam-induced higher order modes. This is perhaps the most self-consistent method of modeling an injector available. An interesting side-effect is that obtaining the actual cavity modes excited by wakefields can be challenging; a PIC code does not "know" about cavity modes, it simply knows the net charge and the electric and magnetic fields at each point of a grid at a given point in time: it will update those fields and particle positions and velocities self-consistently at each time step.

There are several significant disadvantages to PIC codes: first, they tend to be much more computationally intensive to operate, both from a memory and CPU time standpoint, than particle pusher codes of similar dimensionality (*i.e.*, 2-D or 3-D) because Maxwell's equations are being solved on every grid point in the model, whether or not there are macroparticles present.

Mesh generation is still in the realm of an art, and although much progress has been made with automatic mesh generation, it can still be challenging to generate suitable meshes. The difficulty lies in part with the ratio of the size of the beam to the size of the photoinjector, typically on the order of 100:1 in radius and 1000:1 or greater longitudinally. At the outer boundaries of the injector cavities, where no beam particles are liable to be present, the mesh can be relatively coarse; but, to resolve fine structures within the beam, the mesh density in the region of the beam must be relatively high. Thus, a uniform mesh will generally either be too coarse to properly resolve the electron beam, or too fine to allow the simulation to run in a reasonable amount of time and memory. Good progress is being made in non-uniform mesh generation; and concepts involving overlaid meshes are very interesting, but this is also an area of active development.

1.7.4 Other Types of Beam Dynamics Codes

Several other types of injector design codes should be mentioned. First, envelope codes, such as TRACE-3D [1.48] and HOMDYN [1.49], use externally generated, or analytic, fields and a simplified representation of the beam (an $M * N$ grid of charged rings for HOMDYN, or a uniformly filled ellipse for TRACE-3D) to model the injector. Historically these codes have been very valuable as "first step" modeling, however, with the increasing power of desktop computers, particle pusher codes running with small particle counts are nearly as fast in a practical sense and provide an easy method of model refinement by simply increasing the particle count.

Field mode codes represent a compromise between particle pusher and PIC codes. This type of code relies, as does particle pusher codes, upon local PIC grids and externally defined fields. However, the field code "knows" about cavity modes and can calculate the beam's contribution to, and influence from, multiple cavity modes at once. These codes are not currently in widespread use, however.

While many particle pusher codes theoretically incorporate enough accelerator component models to be useful for designing an entire accelerator, often they are used only for the photoinjector region, after which the beam is "handed off" to a high-energy accelerator design code.

High-energy accelerator design codes, such as TRANSPORT [1.34], MAD [1.50], [1.51] and ELEGANT [1.52], originated from the need to design complete accelerators comprising potentially thousands of elements. They typically propagate beam particles or rms envelopes using a 1st-, 2nd- or 3rd-order matrix approach and often incorporate goal-seeking or parameter matching functionality. With certain limited exceptions, they generally do not perform space charge calculations and are therefore not suitable for injector design; however, they often include features critical for high performance accelerator design, such as coherent space charge radiation (CSR) modeling, which are missing from or have limited support in pseudo-PIC codes. Since these codes are often provided input from photoinjector design simulations, it is helpful to be at least somewhat familiar with their requirements and limitations.

1.7.5 Electromagnetic Design Codes and Accelerator Component Modeling

The electromagnetic fields used in particle beam simulations have to come from somewhere. In PIC codes, the fields in an RF cavity (for instance) can often be generated by the PIC code itself. In pseudo-PIC codes, the fields are generally either represented *via* analytic formulas, or are imported as external field maps.

In most photoinjector simulations, the RF fields used to accelerate the beam are provided *via* importing a field map generated by an external code. Critical magnetic elements near the photocathode, such as those generated by emittance compensation solenoid magnets, are also often generated externally and imported as maps. Other magnetic elements, such as dipoles and quadrupoles, often may (or must, depending on the code) be approximated by analytic expressions for “hard-edge” fields.

There are many EM codes available with varying degrees of fidelity, and the topic is well outside the scope of this book. When considering an EM design code, the photoinjector designer should consider both the fidelity with which an EM code will model elements of the injector, and also the ease with which the results of the calculations can be imported into the beam dynamics code. For instance, the POISSON/SUPERFISH codes [1.17] typically only calculate 2-D field maps (*e.g.*, *z-r* maps for RF cavities or solenoids). They are, however, tightly integrated with the POISSON beam dynamics code, and GPT has a number of useful tools to ease importation of field maps from POISSON/SUPERFISH. On the other hand, a “world’s most accurate” electromagnetic design code is of limited utility to the photoinjector designer if it cannot be used to generate the required field maps.

The line between EM codes and PIC codes for beam dynamics is not always well defined. As mentioned above, some beam dynamics codes, such as VORPAL, are capable of generating RF cavity fields. Some EM design codes, such as MAFIA [1.53], [1.1] and CST [1.55], can include electron emission modeling and transport with varying degrees of physical fidelity.

1.7.6 General Approach to Injector Modeling

Injector modeling can be approached in three phases: Conceptual development, tuning and final refinement.

Conceptual development can be performed with any type of injector design code, but the practice in common use as of this writing is to employ a code such as SUPERFISH, to generate radially symmetric acceleration and solenoid fields from simplified models of the injector geometry and use a particle pusher code to perform beam dynamics simulations. This can be used to quickly narrow down on a reasonable parameter space for more detailed exploration.

In tuning, or optimization, many simulations are run to identify optimal working points. Depending upon the sophistication of the optimization techniques used, this step can also adjust injector “physical” parameters, such as cavity length or cathode/anode geometry that are fixed once the injector is built, as well as parameters, such as accelerating gradients and solenoid field strengths, that can be altered without changing the injector's physical construction. Here again, the advantage to particle pusher codes is speed. The combination of fast particle pusher codes with concurrent computing and advanced optimization methods is extremely powerful, as demonstrated by the design of the Cornell ERL injector.

The final refinement of the design incorporates as many physical effects as reasonable, given the available resources and performance requirements. In the case of the LCLS injector, for instance, this stage included using 3-D electromagnetic field maps for both the TM_{010} and TM_{011} (accelerating) modes in the RF gun, quadrupole corrections to the emittance compensation solenoid, *etc.* This can be the most time consuming stage of the simulation process, but as the LCLS injector has demonstrated, the results are definitely worthwhile.

As a final note, it is well worth remembering that no simulation is a complete representation of physical reality. This is because neither the codes nor the researchers are perfect. That is to say, some things aren't in the model because the code doesn't support it; an example would be semiconductor cathodes in PARMELA. We know this and attempt to allow for it when interpreting our simulation results. Other things aren't in the codes because we do not implement them, although the code can support them. An example of this from the NCRF photoinjector design community is the influence of the TM_{010} mode in the SLAC/BNL/UCLA-style RF guns. In practice, the TM_{010} mode can have a noticeable impact on beam quality, but most early design studies did not include its effects in the simulations. As a result, obtaining 1 μm emittance beams at nanocoulomb bunch charges was considerably more challenging than was anticipated from the simulations.

Therefore, we close the section on simulation with two questions to keep in mind:

"What does the simulation not include?" and

"What am I not including that might matter?"

1.8 Conflict of Interest and acknowledgements

The authors confirm that this article content has no conflicts of interest. J. W. Lewellen acknowledges the support of the Office of Naval Research, the High-Energy Laser Joint Technology Office and the Naval Postgraduate School. D. H. Dowell thanks his understanding wife, Alice.

References

[1.1] G. Neal, C. L. Bohn, S. V. Benson *et al.*, "Sustained kilowatt lasing in a free-electron laser with same-cell energy recovery," *Phys. Rev. Lett.*, vol. 84, pp. 662-665, January 2000.

[1.2] P. Emma, R. Akre, J. Arthur *et al.*, "First lasing and operation of an ångstrom-wavelength free-electron laser," *Nature Photonics*, vol. 4, pp. 641-647, August 2010.

[1.3] M. Reiser, *Theory and Design of Charged Particle Beams*, Weinhiem: Wiley-VCH, 2007, pp. 16.

[1.4] C. H. Lee, P. E. Oettinger, R. Klinkowstein *et al.*, "Electron emission of over 200 A/cm^2 from a pulsed-laser irradiated photocathode," *IEEE Trans. Nucl. Sci.*, vol. 32, pp. 3045-3047, October 1985.

[1.5] J. S. Fraser, R. L. Sheffield and E. R. Gray, "High-brightness photoemitter development for electron accelerator injectors," in *Proc. AIP Conf.*, vol. 130, 1985, p. 598-601.

[1.6] J. S. Fraser, R. L. Sheffield and E. R. Gray, "A new high-brightness electron injector for free electron laser," *Nucl. Instrum. Meth. A*, vol. 250, pp. 71-76, September 1986.

[1.7] R. L. Sheffield, "High brightness electron sources," in *Proc. 1995 Particle Accelerator Conf.*, 1995, pp. 882-886.

[1.8] C. Travier, "RF guns: bright injectors for FEL," *Nucl. Instrum. Meth. A*, vol. 304, pp. 285-296, July 1991.

[1.9] D. H. Dowell and J. G. Power, "High-average power facilities," SLAC, Stanford, CA, Technical Report No. SLAC-PUB-15232, September 5, 2012.

[1.10] F. Zhu, S. W. Quan, J. K. Hao *et al.*, "Status of the DC-SRF photoinjector for PKU-SETF," in *Proc. 2011 Superconducting RF*, 2011, pp. 973-976.

[1.11] D. Janssen, V. Volkov, H. P. Bluem and A. M. M. Todd, "Axial RF power input into photocathode electron guns," in *Proc. 2005 Particle Accelerator Conf.*, 2005, pp. 743-745.

[1.12] R.A. Rimmer, "A high-gradient cw RF photo-cathode electron gun for high current injectors," in *Proc. 2005 Particle Accelerator Conf.*, 2005, pp. 3049-3051.

[1.13] H. Bluem, "High power testing of a fully axisymmetric rf gun," in *Proc. 2007 Particle Accelerator Conf.*, 2007, pp. 3142-3144.

[1.14] J. W. Staples, K. M. Baptiste, J. N. Corlett *et al.*, "Design of a vhf-band photoinjector with megahertz beam repetition rate," in *Proc. 2007 Particle Accelerator Conf.*, 2007, pp. 2990-2992.

[1.15] D. Kayran and V. N. Litvinenko, "Novel method of emittance preservation in ERL merging system in presence of strong space charge forces," in *Proc. 2005 Particle Accelerator Conf.*, 2005, pp. 2512-2514.

[1.16] D. Kayran and V. N. Litvinenko, "A method of emittance preservation in ERL merging system," in Proc. 27th Int. Free Electron Laser Conf., 2005, pp. 644-647.

[1.17] J. H. Billen and L. M. Young, "Poisson SUPERFISH," Los Alamos National Laboratory, Technical Report LA-UR-96-1834, updated 2003.

[1.18] K-J. Kim, "RF and space-charge effects in laser-driven rf electron guns," *Nucl. Instrum. Meth. A*, vol. 275, pp. 201-218, February 1989.

[1.19] D. H. Dowell, M. Ferrario, T. Kimura *et al.*, "A two-frequency RF photocathode gun," *Nucl. Instrum. Meth. A*, vol. 528, pp. 316-320, August 2004.

[1.20] D. H. Dowell, T. D. Hayward and A. M. Vetter, "Magnetic pulse compression using a third harmonic RF linearizer," in *Proc. 1995 Particle Accelerator Conf.*, 1995, pp. 992-994.

[1.21] X. J. Wang, X. Qiu and I. Ben-Zvi, "Experimental observation of high-brightness microbunching in a photocathode rf electron gun," *Physical Review E*, vol. 54, pp. 3121-3124, October 1996.

[1.22] M. Reiser, *Theory and Design of Charged Particle Beams*, Weinhiem: Wiley-VCH, 2007, pp. 10.

[1.23] J. Rosenzweig, N. Barov, S. Hartman *et al.*, "Initial measurements of the UCLA RF photoinjector," *Nucl. Instrum. Meth. A*, vol. 341, pp. 379-385, March 1994.

[1.24] M. Reiser, *Theory and Design of Charged Particle Beams*, Weinhiem: Wiley-VCH, 2007, Section 6.2.1.

[1.25] F. Zhou, I. Ben-Zvi, M. Babzien *et al.*, "Experimental characterization of emittance growth induced by the nonuniform transverse laser distribution in a photoinjector," *Phys. Rev. ST Accel. Beams*, vol. 5, pp. 094203-1–094203-6, September 2002.

[1.26] A. Brachmann, R. N. Coffee, D. H. Dowell *et al.*, "LCLS drive laser shaping experiments," in *Proc. 2009 Free Electron Laser Conf.*, 2009, pp. 463-465.

[1.27] T. Wangler, *RF Linear Accelerators*, Weinhiem: Wiley-VCH, 1998, pp. 283-285.

[1.28] B. E. Carlsten, "New photoelectric injector design for the Los Alamos National Laboratory XUV FEL accelerator," *Nucl. Instrum. Meth. A*, vol. 285, pp. 313-319, December 1989.

[1.29] L. Serafini and J. Rosenzweig, "Envelope analysis of intense relativistic quasilaminar beams in RF photoinjectors: a theory of emittance compensation," *Phys. Rev. E*, vol. 55, pp. 7565-7590, June 1997.

[1.30] M. Ferrario, J. E. Clendenin, D. T. Palmer *et al.*, "HOMDYN study for the LCLS RF photo-injector," SLAC, Stanford, CA, Technical Report No. SLAC-PUB-8400, March 2000.

[1.31] M. Ferrario, D. Alesini, M. Bellaveglia *et al.*, "Direct measurement of the double emittance minimum in the beam dynamics of the sparc high-brightness photoinjector," *Phys. Rev. Lett.*, vol. 99, pp. 234801-1–234801-5, December 2007.
[1.32] J. F. Schmerge, J. Castro, J. E. Clendenin *et al.*, "The s-Band 1.6 cell RF gun correlated energy spread dependence on π and 0 mode relative amplitude," in Proc. 46th Workshop INFN ELOISATRON Project, 2005, pp. 375-382.
[1.33] M. Reiser, *Theory and Design of Charged Particle Beams*, Weinhiem: Wiley-VCH, 2007, pp. 214.
[1.34] D. C. Cary, K. L. Brown and F. Rothhacker, "Third-order TRANSPORT with MAD input: a computer program for designing charged particle beam transport systems," SLAC, Stanford, CA, Technical Report No. SLAC-Report-530, April 1998, pp. 161.
[1.35] GPT: General Particle Tracer, ver. 2.82, Pulsar Physics.
[1.36] M. Reiser, *Theory and Design of Charged Particle Beams*, Weinhiem: Wiley-VCH, 2007, pp. 106-107.
[1.37] M. Born and E. Wolf, *Principles of Optics: Electromagnetic Theory of Propagation Interference and Diffraction of Light*, 6th Ed., pp. 217, Oxford: Pergamon Press, 1980.
[1.38] D. H. Dowell, E. Jongewaard, J. Lewandowski *et al.*, "The development of the linac coherent light source RF gun," *Beam Dynamics Newslett.*, No. 46, pp. 162-192, August 2008.
[1.39] R. Akre, D. H. Dowell, P. Emma *et al.*, "Commissioning the linac coherent light source injector," *Phys. Rev. ST Accel. Beam*, vol. 11, pp. 030703-1–030703-20, March 2008.
[1.40] L. Serafini, "Short bunch blow-out regime in RF photoinjectors," in *AIP Conf. Proc.*, vol. 413, 1997, pp. 321-334.
[1.41] O. J. Luiten, S. B. van der Geer, M. J. de Loos *et al.*, "How to realize uniform three-dimensional ellipsoidal electron bunches," *Phys. Rev. Lett.*, vol. 93, pp. 094802-1–094802-4, August 2004.
[1.42] L. M. Young, "PARMELA documentation," Los Alamos National Laboratory, Los Alamos, NM, Technical Report No. LA-UR-96-1835 (Revised June 8, 2004).
[1.43] L. M. Young, private communication.
[1.44] J. Qiang, I. V. Pogorelov and R. Ryne, "Recent improvements to the IMPACT-T parallel particle tracking code," in *Proc. 2006 Int. Computational Accelerator Physics Conf.*, 2006, pp. 185-187.
[1.45] J. Qiang, "IMPACT-T User Document Version 1.5," LBNL, Berkeley, CA, Technical Report No. 62326, 2007.
[1.46] K Flöettmann. (2011). ASTRA-Manual_V3 [Online]. Available: FTP: http://www.desy.de Directory: ~mpyflo/Astra_dokumentation/ File: ASTRA-Manual_V3.pdf.
[1.47] C. Nieter and J. R. Cary, "VORPAL – a multidimensional code for simulating advanced accelerator concepts," in *Proc. 2001 Particle Accelerator Conf.*, 2001, pp. 3105-3107.
[1.48] D. P. Rusthoi, W. P. Lysenko and K. R. Crandall, "Further improvements in TRACE 3-D," in *Proc. 1997 Particle Accelerator Conf.*, 1997, pp. 2574-2576.
[1.49] M. Ferrario. (1999). HOMDYN user guide [Online]. Available: FTP: http://nicadd.niu.edu Directory: fnpl/hondyn/ File: manual.pdf.
[1.50] F. C. Iselin, J. M. Jowett, J. Pancin *et al.*, "MAD version 9," in *Proc. 2000 European Particle Accelerator Conf.*, 2000, pp. 1042-1044.
[1.51] The Methodical Accelerator Design Group Home page. Available Online: http://mad.web.cern.ch/mad/.
[1.52] M. Borland, V. Sajaev, H. Shang *et al.*, "Recent progress and plans for the code elegant," in *Proc. 2009 Int. Computational Accelerator Physics Conf.*, 2009, pp. 111-116.
[1.53] F. Ebeling, R. Klatt, F. Karawzcyk *et al.*, "Status and future of the 3D MAFIA group of codes," in *Proc. 1988 European Particle Accelerator Conf.*, 1988, pp. 279-281.

[1.54] S. Setzer, R. Cee, M. Krassilnikov *et al.*, "FEL photoinjector simulation studies by combining MAFIA TS2 and ASTRA," in *Proc. 2002 European Particle Accelerator Conf.*, 2002, pp. 1664-1666.

[1.55] MicroWave Studio, ver. 4.2, available by Computer Simulation Technology GmbH, Bad Nauheimer Str. 19, 64289 Darmstadt, Germany. Available at www.cst.com/Content/Products/MWS/Overview.aspx.

Appendix 1.1: Useful Formulae

Emittance type	Emittance formula
Intrinsic (a.k.a. thermal)	$\varepsilon_{n,\text{intrinsic}} = \beta\gamma\sqrt{\frac{\hbar\omega-\phi_{eff}}{3mc^2}}$
Surface Roughness (High Field Enhancement)	$\varepsilon_{n,field} = \sigma_x \frac{\left\langle v_x^2\right\rangle^{1/2}}{c} = \sigma_x\sqrt{\frac{\pi^2 a_n^2 eE_a}{2\lambda_n mc^2}}$
Space Charge Emittance for Gaussian Distributions	$\varepsilon_{n,sc} = \frac{\pi}{4}\frac{1}{\alpha k_z \sin\phi_0}\frac{I}{I_0}\frac{1}{3A_{gaus}+5}$ $\mathrm{A}_{gaus} = \frac{\sigma_x}{\sigma_z}$
Space Charge Emittance for Uniform Cylindrical Distribution	$\varepsilon_{n,sc} = \frac{\pi}{4}\frac{1}{\alpha k_z \sin\phi_0}\frac{I}{I_0}\frac{1}{35\sqrt{A_{cyl}}}$ $\mathrm{A}_{cyl} = \frac{a}{l}$
Non-uniform Emission Space Charge Emittance	$\varepsilon_{n,sc}(\Delta I_{bunch}) = \sigma_x \frac{2}{n_s}\sqrt{\frac{2}{\pi}\frac{\Delta I_{bunch}}{I_0}}$
1st-order RF emittance	$\varepsilon_{n,1rf} = \frac{eE_0}{2mc^2}\left\|\cos\phi_e\right\|\sigma_{x,e}^2\sigma_\phi$
2nd-order RF emittance	$\varepsilon_{n,2rf} = \frac{eE_0}{2\sqrt{2}mc^2}\left\|\sin\phi_e\right\|\sigma_{x,e}^2\sigma_\phi^2$
Geometric Emittance	$\varepsilon_{n,geo} = 0.0046\left(\mu m/mm^4\right)\sigma_{x,sol}^4$
Chromatic Emittance	$\varepsilon_{n,chromatic}(\sigma_{x,sol}) = \beta\gamma\sigma_{x,sol}^2 K\left\|\sin KL + KL\cos KL\right\|\frac{\sigma_p}{p}$
Anomalous Quadrupole Field Emittance	$\varepsilon_{n,quad-sol}(\sigma_{x,sol}) = \beta\gamma\sigma_{x,sol}^2\left\|\frac{\sin 2KL}{f_q}\right\|$

Appendix 1.2: Mathematical Symbols

Symbol	Definition	Value
α	Electric Field Parameter, $\alpha \equiv \frac{eE_0}{2mc^2 k_z}$	-
β	Velocity divided by Speed of Light, $\beta = \frac{v}{c}$	-
c	Speed of Light in Vacuum, $c = \frac{1}{\sqrt{\varepsilon_0 \mu_0}}$	2.99×10^{8} m/s
δ_{skin}	Skin Depth of the Transverse RF Field, $\delta_{skin} = \sqrt{\frac{2}{\sigma_{wall}\, \mu_0\, \omega_{RF}}}$	-
ε_0	Electric Permittivity of Vacuum	8.85×10^{-12} C/V-m, 5.526×10^{7} e/V-m
μ_0	Magnetic Permeability of Vacuum	-
γ	Total Energy Normalized to the Electron Rest Mass	-
m	Rest Mass of the Electron	0.511 MeV/c^2
ϕ_{eff}	Effective Work Function for Photoemission, $\phi_{eff} = \phi_W - \phi_{schottky}$	
ϕ_W	Material Work Function for Photoemission	~4.6 eV for Cu
$\phi_{Schottky}$	Schottky Work Function due to Image Charge and Field, $\phi_{schottky} = 3.7947\times10^{-5}\sqrt{E(V/m)}$ eV	-
ε_{n}	Normalized Emittance	-
σ_x	Transverse rms Beam Size	-
σ_{wall}	Conductivity of Cavity Walls	-
υ_x	Velocity along the x-coordinate	-
σ_z	Longitudinal rms Beam Size	-
$\sigma_{x,e}$	Transverse rms Beam Size at Exit of RF Gun	-
$\sigma_{x,sol}$	Transverse rms Beam Size in the Solenoid	-
σ_p	Bunch rms Momentum Spread	-
σ_ϕ	rms Phase Length of Bunch	-
ϕ_0	Initial Launch Phase of the Electron relative to the RF Waveform	-
ϕ_e	Beam RF Phase when Bunch is at Exit of Gun	-
ω, ω_{rf}, ω_{RF}	RF Angular Frequency, $\omega = 2\pi f$	-
p	Bunch Average Momentum	-
a_n	Amplitude of n^{th} Spatial Frequency of the Surface Roughness	-
e	Electron Charge	1.6×10^{-19} C
E_a	Applied or External Electric Field, usually RF or HV DC.	-
E_0	Peak Field at Cathode	-
λ_n	Spatial Wavelength of Surface Modulation with Wave Number k_n	-

Symbol	Definition	Value
k_z	Longitudinal RF Wave Number, $k_z = \frac{p\pi}{l}$, where l is the Cavity length; also, $k_z = \frac{2\pi}{\lambda_{rf}}; c = \lambda_{rf} f_{rf}$ for Standing Wave Cavity	-
E_K	Kilpatrick Criterion Peak Field	-
I	Beam Current, usually the Peak Current	-
I_0	Characteristic Current for Electrons, $I_0 = ec\, r_e^{-1} \approx 17$ kA	-
A_{gaus}	Aspect Ratio for Gaussian Bunch Shape, $\mathrm{A}_{gaus} = \frac{\sigma_x}{\sigma_z}$	-
A_{cyl}	Aspect Ratio for a Uniform Cylinder Bunch, $\mathrm{A}_{cyl} = \frac{a}{l}$	-
a	Radius of Cylindrical Bunch	-
l	Length of Cylindrical Bunch	-
ΔI_{bunch}	difference of max and min local current of transverse spatial modulation	-
n_s	Number of Spatial Modulations across the Beam Diameter	-
K	Focal Strength of Solenoid, $K = \frac{eB_{sol}}{2p} = \frac{B_{sol}}{2(B\rho)_0}$	-
L, L_{sol}	Solenoid Magnetic Length	-
f_q	Quadrupole Focal Length, usually for Solenoid Quadrupoles	-
f_{RF}, f_{rf}	Radiofrequency (RF) in Hertz	-
Q	Quality Factor of Resonant System, $Q = \frac{(Stored\ Energy)}{(Dissipated\ Energy)}$	-
r_{shunt}	Shunt Impedance for RF Power and Cavity Voltage, $r_{shunt} = \frac{V_0^2}{P}$	-
V_0	Cavity Voltage	-